

# Acoustic AESA Project 1

---

Transmitter Design and Analogue Beamforming



Presented by:  
Kieran Cattell

Prepared for:  
W. P. F Schonken  
Dept. of Electrical and Electronics Engineering  
University of Cape Town

Submitted to the Department of Electrical Engineering at the University of Cape Town  
in partial fulfilment of the academic requirements for a Bachelor of Science degree in  
Mechatronics

October 13, 2019

**Key words:** Radar, AESA, Phase Shift, Beamforming, Transducer, Phased Array



## Declaration

---

1. I know that plagiarism is wrong. Plagiarism is to use another's work and pretend that it is one's own.
2. I have used the IEEE convention for citation and referencing. Each contribution to, and quotation in, this report from the work(s) of other people has been attributed, and has been cited and referenced.
3. This report is my own work.
4. I have not allowed, and will not allow, anyone to copy my work with the intention of passing it off as their own work or part thereof.



Signature:

Kieran Cattell

Date:

October 13, 2019.

## Acknowledgments

---

I would like to acknowledge the following people who have helped or supported me throughout this project.

My supervisor, Dr Francois Schonken, for the support and guidance whenever it was needed. Much of this project would not have been possible without his expertise.

Brendan Daniels for providing components no matter how often I asked and Justin Pead for component and PCB orders.

I would like to thank my parents for their love and support throughout my life. I also appreciate the multiple attempts at trying to show interest in this project despite your limited understanding of the topic.

I would also like to thank Stefan Dominicus, Jonti Oehley, Irshaad Dodia and Alan Pohl who have kept me sane and on the right track throughout my years at UCT.

## Abstract

---

This project covers the design and testing of a phased array ultrasonic transducer creating an acoustic AESA. The report looks at the beamforming and phase shifting using analogue techniques. This requires the report to cover the design and simulation of the phase shifters, the transducer driver circuits and the beamforming using the transducers. The report then covers the construction and testing of the built array and discusses the performance.

# Contents

<b>1</b>	<b>Introduction</b>	<b>1</b>
1.1	Background . . . . .	1
1.2	Objectives of the Study . . . . .	2
1.2.1	Problems to be Investigated . . . . .	2
1.2.2	Purpose of the Study . . . . .	3
1.3	Scope & Limitations . . . . .	3
1.4	Plan of Development . . . . .	4
<b>2</b>	<b>Literature Review &amp; Development of Theory</b>	<b>5</b>
2.1	AESA Radar & Phased Arrays . . . . .	5
2.1.1	AESA Antennae . . . . .	6
2.1.2	Theory of Phased Arrays . . . . .	6
2.2	Ultrasonic Imaging . . . . .	7
2.3	Analogue Beamforming . . . . .	8
2.4	Analogue Phase Shifting . . . . .	9

2.4.1	All-Pass Filter . . . . .	10
2.4.2	Analogue Delay . . . . .	11
<b>3</b>	<b>Subsystem Design, Testing &amp; Integration</b>	<b>13</b>
3.1	Design of Phase Shifting Units . . . . .	13
3.1.1	Potential Solutions . . . . .	13
3.1.2	Circuit Design & Testing . . . . .	20
3.2	Design of Transducer Driver Circuits . . . . .	23
3.2.1	Requirements of Transducer Driver Circuits . . . . .	23
3.2.2	Theory & Simulations . . . . .	23
3.2.3	Breadboard & Veroboard Design . . . . .	27
3.3	Beamforming . . . . .	29
3.3.1	Beamforming with Ideal Transducers . . . . .	29
3.3.2	Beamforming with Non-Ideal Transducers . . . . .	29
3.4	Integration of Subsections . . . . .	32
3.5	Test Rig & Procedure . . . . .	34
<b>4</b>	<b>Results</b>	<b>36</b>
4.1	Simulation Results . . . . .	36
4.2	Experimental Results . . . . .	37
<b>5</b>	<b>Discussion</b>	<b>40</b>

5.1	Simulated Results Compared to Theory . . . . .	40
5.2	Experimental Results Compared to Simulations . . . . .	41
5.2.1	Beam Angle . . . . .	41
5.2.2	Beamshape . . . . .	43
5.3	Performance of the Array . . . . .	44
<b>6</b>	<b>Conclusions</b>	<b>45</b>
<b>7</b>	<b>Recommendations</b>	<b>47</b>
<b>References</b>		<b>48</b>
<b>A</b>	<b>SPICE Models</b>	<b>50</b>
A.1	Phase Shifting Units . . . . .	50
A.2	Driver Circuitry . . . . .	51
<b>B</b>	<b>Schematics and Layouts</b>	<b>52</b>
B.1	Schematics . . . . .	52
B.2	Breadboard Layouts . . . . .	53
B.3	PCB and Veroboard Layouts . . . . .	53
<b>C</b>	<b>Additional Results &amp; Resources</b>	<b>54</b>
C.1	Simulation Results . . . . .	54
C.2	Experimental Results . . . . .	56

C.3 Comparisons . . . . .	58
C.4 Test Rig Laser Cutting Template . . . . .	61
C.5 JFET Matching Circuit . . . . .	62
<b>D MATLAB Code</b>	<b>63</b>
<b>E Ethics Form</b>	<b>64</b>

# List of Figures

2.1	Example of a phased array where each element can be seen to have both a phase shift and attenuation unit. Image taken from [1] . . . . .	6
2.2	Phase Shifting unit using co-axial delay lines. Taken from [2] . . . . .	9
2.3	An Active First-Order All-Pass Filter. The output phase will lead the phase of the input. . . . .	10
2.4	Phase Response of All-Pass Filter shown in Figure 2.3 where $f_0 = 40\text{kHz}$	11
3.1	Clock Frequency vs Delay Time for the Panasonic MN series of BBDs taken from the datasheet [3]. The curves for the MN3012 and MN3007 have been highlighted in green and yellow respectively. . . . .	14
3.2	Schematic for All-Pass Filter capable of shifting a 40kHz sinusoid from $0^\circ$ to $360^\circ$ based on the voltage of the control signal. . . . .	16
3.3	Simulated output for the phase shifting units shown in 3.2 with the JFETs modelled as an open circuit. The output can be seen to be in phase with and overlapping the input. . . . .	17
3.4	Simulated output for the phase shifting units shown in 3.2 with the JFETs modelled as a short circuit. The output can be seen to be $360^\circ$ out of phase and overlapping the input. . . . .	17
3.5	Simulated output for the phase shifting units shown in 3.2 with the control voltage swept from $-2V$ to $-3V$ . The output can be seen shifting from $0^\circ$ to $360^\circ$ . Additionally, some attenuation to the signal as well as a DC offset can be observed as the signal transitions. . . . .	18

3.6	Isolated voltage divider . . . . .	18
3.7	Simulated relationship between control voltage and phase shift. The curve can be seen to have two roughly linear regions. . . . .	19
3.8	Tested relationship between control voltage and phase shift . . . . .	21
3.9	Simulated output of an LM741 used as a comparator at 40kHz . . . . .	24
3.10	LM311 internal topology showing BJT output stage. Image taken from LM311 datasheet [4]. . . . .	25
3.11	Simulated output of LM741 used as a comparator as well as the LM311 at 40kHz. . . . .	25
3.12	Schematic for transducer driver circuitry . . . . .	26
3.13	Simulated output of LM311 at 40kHz with 2000pF load. . . . .	26
3.14	Simulated output transducer driver with load . . . . .	27
3.15	Experimental output of transducer driver without load . . . . .	27
3.16	Experimental output of transducer driver with load . . . . .	28
3.17	Simulated beamshape of four in-phase elements with $\frac{\lambda}{2}$ , $\lambda$ and $2\lambda$ spacing. Note that for the $\frac{\lambda}{2}$ case the grating lobes are roughly a quarter the amplitude of the main beam while in the other two cases the grating lobes are the same amplitude as the main beam. Additionally, the number of grating lobes roughly doubles as the spacing does. . . . .	30
3.18	Measured size of unmodified and modified transducer . . . . .	31
3.19	Beam of modified and modified transducers. The modifications to the transducer result in added grating lobes and attenuation. . . . .	31

3.20 Simulated Beam of four modified transducers. The simulation shows a single main beam with small grating lobes. The black trace shows the response of omnidirectional transducers showing the beam angle prevents the formation of the large grating lobes. . . . .	32
3.21 Possible configuration 1 . . . . .	33
3.22 Possible configuration 2 . . . . .	34
3.23 Transducer array mounted onto the rotating platform allowing . . . . .	35
4.1 Simulated and theoretical results of the array . . . . .	37
4.2 Example of measured data and corresponding Fourier Transform . . . . .	38
4.3 Transducer array mounted onto the rotating platform allowing a 180° sweep in 5° increments . . . . .	39
5.1 Simulated and experimental results of the array . . . . .	42

# List of Tables

5.1	Comparison of theoretical results to simulated results . . . . .	41
5.2	Comparison of experimental results to simulated results . . . . .	42
5.3	Comparison of experimental results to simulated results . . . . .	43
5.4	Cross-correlation between simulated and measured results . . . . .	44

# Chapter 1

## Introduction

### 1.1 Background

An active electronically scanned array (AESA) is a phased array antenna which, by shifting the relative phase of each element within the array, can steer the direction of the transmitted beam without any physical movement of the antenna [1].

While a directional antenna can be created and steered mechanically, phased arrays allow for the beam to be scanned at electronic speeds. Additionally, by the manipulation of the phase of each element, the array can output several main beams [1]. Electronic systems are also less prone to wear and tear than that of mechanical systems, which, with the beamforming flexibilities, make phased arrays very versatile.

While AESA antennae usually emit radio waves as part of an active phased array radar (APAR), the constructive and destructive interference which shapes the beam can be applied to other mediums such as, in the case of this project, acoustic waves.

To steer the beam, each element in the array requires its an individual phase-shifting unit [1]. In radar applications at high frequencies, both analogue and digital phase-shifters can be used. However, the aim of this project is for the control circuitry to be completely analogue and at the relatively low frequency of ultrasound, achieving this phase shift is significantly more challenging. Since ultrasonic frequencies are closer to audio frequencies than those of radar, techniques used in typical audio processing effects such as phasers and delays can be used to employ the phase shifts.

## CHAPTER 1. INTRODUCTION

A benefit to using acoustic waves for a phased array is the cost. While radar-based AESA systems are a common feature of ships and aircraft, the required antennae are not affordable to small scale applications. Additionally, acoustic waves have no adverse effects on the human body [5]. This allows ultrasonic phased arrays to be used in affordable noninvasive medical imaging applications.

## 1.2 Objectives of the Study

The objectives of this report can be divided into the problems which need to be solved as well as the purpose of the study.

### 1.2.1 Problems to be Investigated

The main two areas of investigation for the study are the analogue phase shifting and the beam formation.

Existing examples of analogue phase shifting can be found in audio processing applications [6, 7]. An audio phaser sums the original signal and a variably phase-shifted signal to create a sweeping filter. Additionally, as the system only works on a single frequency, a phase shift could be achieved using a variable analogue delay.

Beamforming with ultrasonic transponders poses two potential challenges. Firstly, ultrasonic transponders, unlike radar antennae, are strictly directional and have a specified beam angle [8]. This restricts the range of the beam as well as possibly causing unexpected lobes to the beam as a result of elements being unable to destructively interfere with the waves of other elements.

Secondly, the ratio of the physical size of the element to wavelength is much larger for ultrasonic transducers as it is to electromagnetic antennae. This can restrict the distance between elements.

### 1.2.2 Purpose of the Study

This study aims to demonstrate that it is possible to create an AESA-type ultrasonic array which can scan a beam. While the aim of this is to allow the array to be used for short-distance ranging and detection purposes, the theory behind the construction of the array allows for the technology to be expanded to be used in medical imaging applications or long-range applications.

The reasoning behind the creation of an 'acoustic AESA' is to allow for a low cost electronically controlled SONic Detection And Ranging (SODAR) device for use when the cost of a radar system becomes significant.

While the problem can be solved digitally, the analogue nature of the beamforming of this project allows for low-cost scalability. With digital beamforming, a phase-shifted waveform would need to be created for each element in the array, which requires as many GPIO pins of the microcontroller as elements in the array. While for the small array size and low frequencies investigated in this report affordable microcontrollers (such as Arduino, Teensy or STM32) can handle the task easily, as the array size and frequency of the array are increased affordable microcontrollers are unable to achieve the task.

The solution proposed by this investigation will allow for the array to run off of a single feed network with either a single analogue voltage or as many analogue voltages as elements. While the latter appears to suffer from the same scalability limitations, the voltage required is a single DC voltage allowing for affordable microcontrollers with comparatively cheap digital to analogue converters (DAC) to be used.

## 1.3 Scope & Limitations

In order to make use of a phased array, a phased transmitter, as well as a receiver, are needed. The scope of this investigation lies solely in the design and construction of the transmitter array. Additionally, the array size investigated in this report consists of four elements. While this array size limits the performance of the array, it should be sufficient to show that the subsections work as designed and be able to steer the direction of a beam.

## 1.4 Plan of Development

This report slightly deviates from a standard report template. This is due, in part, to a lack of similar projects. While work has been done in ultrasonic phased arrays, this is rarely used in ranging and detection and less so using analogue beamforming. This lead to the literature review being combined with the theory section to allow for theory to supplement any areas missing from the literature.

Chapter 2 of this report consists of the literature review and the development of theory. This section outlines the main areas of the problem at hand and gains insight into the past approaches taken to achieve the required goals.

Chapter 3 breaks down the design of the array into three broad areas. Firstly, the design, simulation and testing of the phase shifting units is conducted. This begins by looking at how the problem could be solved before deciding on the most viable solution. This phase shifter was then simulated and built with the experimental results being compared to the simulations.

The second part of the chapter looks at the amplifier and driver circuitry that powers the transducers. Again this section looks at multiple solutions before selecting the most applicable and designing, simulating and testing the result. The third part looks at the beamforming of the array and the necessary physical construction. The chapter concludes by integrating the three subsystems into the final configuration and discussing the required test rig and test procedure.

Chapter 4 looks at the results of the system as a whole. First, the simulated results are gathered before the constructed array was experimentally tested. Chapter 4 also details the acquisition of the data from the test rig.

Chapter 5 of the report forms the discussion of the performance of the array. This is done by first comparing the simulated results with the expected results as determined by the theory and then by comparing the simulated results against the experimental results. The chapter concludes by discussing the performance of the array.

Chapter 6 draws conclusions of the results, as well as the report as a whole before recommendations for further studies are suggested in Chapter 7.

# Chapter 2

## Literature Review & Development of Theory

This section aims to gain an understanding of what similar work has previously been done in the field and the theory behind concepts required for the completion of this project. By understanding the methods and results of similar past projects, this project is able to analyse how the past methodologies may impact the task.

While there is a large amount of literature on AESA and phased arrays using radar as well as ultrasonic phased arrays for use in medical imaging, these projects operate at vastly different frequencies to what is available to this project and thus, while this section attempts to cover as much of the available literature as possible, any missing information is supplemented from the theory.

### 2.1 AESA Radar & Phased Arrays

An AESA radar differs from a usual phased array in that an AESA antenna consists of a solid-state transmitter/receiver module per element in the array. This allows each element in the array to be used as both a transmitter as well as a receiver. As this project just focuses on the transmitting side of the array, technically, this project is just a phased array transmitter.

### 2.1.1 AESA Antennae

Nevertheless, AESA and other phased array antennae are commonplace in both civilian and military applications due the reliability, stealth and multiple functions [2, 9]. Throughout the years of development it has been found that the performance of a phased array increases and the frequency does. In addition to this, as the frequency increases, the wavelength decreases meaning that each element needs to be closer to its neighbours. This requires the physical size of each element to decrease [9].

### 2.1.2 Theory of Phased Arrays

As the technology behind modern AESAs is often kept as military secrets, this section will look at the theory behind phased arrays to gain insight into the design of this project. Figure 2.1 shows an example of the receiver side of a phased array.

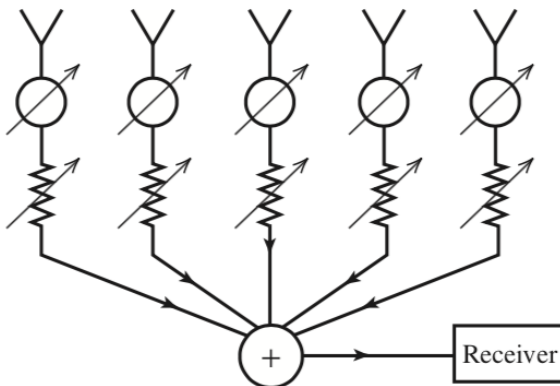


Figure 2.1: Example of a phased array where each element can be seen to have both a phase shift and attenuation unit. Image taken from [1]

The Array Factor (AF) of any array antenna is a function of the relative phases and amplitudes of each element in the array. The AF describes how each element affects the output of the array in polar co-ordinates. The AF is the complex sum of the elements and their respective phase shifts.

$$AF(\theta) = I_0 + I_1 e^{j\beta d \cos(\theta)} + I_2 e^{j\beta 2d \cos(\theta)} = \sum_{n=0}^{N-1} I_n e^{j\beta n d \cos(\theta)} \quad (2.1)$$

where  $I_n = A_n e^{jn\alpha}$  is the complex magnitude ( $A_n$ ) and phase( $\alpha$ ) of the n-th element of the array,  $\beta = \frac{2\pi}{\lambda}$  and  $d$  is the distance between elements [1].

From this it can be seen that as the amplitude and phase of each element can control the

directional output of the array.

In the case of a uniformly excited, equally spaced linear array, the required phase shift between elements can be determined by

$$\phi = \frac{360^\circ d \sin(\theta_{beam})}{\lambda} \quad (2.2)$$

where  $\phi$  is the relative phase shift,  $d$  is the distance between elements, and  $\theta_{beam}$  is the desired beam angle.

The intricacies of phased arrays as used in radar applications do not particularly relate to the scope of this project. Because of this, this literature review will not look at any past projects in this field and will, however, look at the application of ultrasonic phased arrays.

## 2.2 Ultrasonic Imaging

The primary use of ultrasonic imaging is in medical applications as a non-intrusive method of imaging medical patients [10, 11, 12]. Despite this, the methods and approaches used in medical applications can be applied to any ultrasonic imaging problems.

Ultrasonic imaging is largely based around an array of transducers which allow for much quicker imaging over a large area or volume than mechanical scanning allows. Phased arrays of transponders are able to dynamically focus in the direction of the main beam allowing for a 3-dimensional image from the array. This is achieved by varying the electronic focal length while the imaging is taking place [10]. Ultrasonic arrays have also been used to treat deep seated tissue. An ultrasonic phased array can be used to cause cell death in targeted areas as a method of treatment. By steering the beam (or multiple beams) to the desired locations, the array can be moved over the problem areas in order to cause cell death. In a study conducted by Douglas Daum and Kullervo Hynynen, a 256-element ultrasonic array was demonstrated to cause the desired cell death as a result of up to 16 individual beams. The ultrasonic frequency was selected to be 1.1 MHz as a midpoint between cavitation at low frequencies and attenuation at high frequencies [12].

Imaging arrays have limitations in medical applications associated with the depth at which they are able to penetrate. This is as a result of increased attenuation associated with a deeper scan requiring a longer wavelength and diffraction problems associated

with this [10].

While medical imaging applications are designed so that each transducer only receives a reflection from its own transmission, in the case of a ranging and detection applications, each transducer is placed as to allow the reflection to be received by all of the transducers [10].

Unlike the medical imaging applications which are unable to operate at low frequencies due to the nature of human tissue, ranging and detection applications do not suffer from this. This allows more affordable low-frequency ultrasonic transponder to be used in this project.

## 2.3 Analogue Beamforming

The beamforming of the array is achieved both by the control of the phase and attenuation of the individual elements as well as the placement of each element.

Depending on the requirements of the beam, different arrangements of the elements can be used. A simple linear array consists of all the elements in a single axis, however, 2-dimensional arrays such as rectangular arrays, concentric and annular ring arrays and other arrangements can be used in order to steer the beam in spherical co-ordinates rather than polar [10]. This project focuses on a linear array, however, the subsections will be designed allowing for the further studies to be expanded into other configurations.

Many medical applications used digital beamforming in order to control the beam [11, 13]. While this allows for greater control over the large scale of the medical arrays, this is outside the scope of this project. The analogue approach is focussed around the use of Delay and Sum (DS) modules for receiving. On the transmitter side, this is represented by a phase shift of each element. As seen in (2.1) above, by changing the phase of each element the direction and size of the beam can be determined [1, 13].

The spacing of the elements determines the width of the beam with a closer spacing resulting in a wider beam, however, as the elements are distanced from each other, the beam narrows but side lobes are created. These side lobes are known as *grating lobes*. Again this is determined as a result of (2.1) [1, 13].

Using (2.1), the spacing of the elements can be chosen in order to achieve maximum

cancellation resulting in a single main beam. In order for the beam to cancel out in the axis which the transmitters are mounted in, the phase shift of each adjacent element needs to be  $180^\circ$  to completely destroy the effect of the waves. The physical position of each element being a single wavelength apart results in a wave with a  $360^\circ$  phase shift. By placing the elements half a wavelength apart, the phase shift is  $180^\circ$  and the waves cancel each other's effects [1].

This half-wavelength spacing is the furthest spacing which does not result in significant grating lobes.

## 2.4 Analogue Phase Shifting

To achieve the phase shift required to steer the beam of the phased array, each element needs its own phase shifting unit [1]. While it is possible to generate a separate phase-shifted waveform using many digital to analogue converters (DAC), to keep with the scope of the project, the phase-shifters used in this project must be analogue.

Early AESA antennae achieved a phase shift by using delay lines of co-axial cable which can be switched into the signal path. The lengths of each stage is double that of the previous stage allowing the delay lines to be compounded in a binary-like fashion. These delay lines delay the sinusoidal signal providing a phase shift. While this method does achieve a phase shift, there is significant loss as through the co-axial cable resulting in attenuation. Moreover, the delay of the cable is as a result of the resistance which is highly dependent on the temperature [2]. Figure 2.2 shows the an example of phase shifters using delay lines.

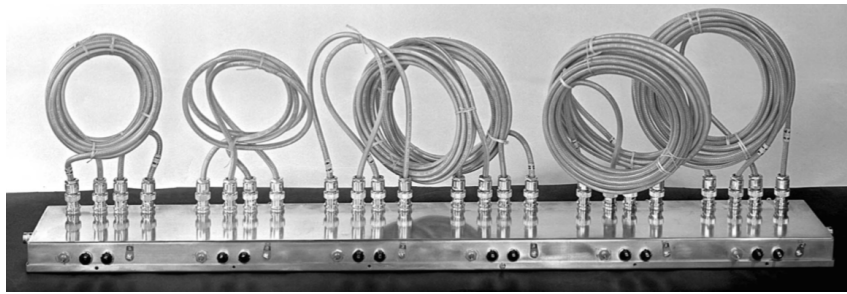


Figure 2.2: Phase Shifting unit using co-axial delay lines. Taken from [2]

Additional drawbacks of using delay lines for this project is the non-continuous nature and the length of the line required. At the lower frequencies of ultrasound, the same delay has a significantly smaller effect on the phase resulting in more cable and thus

more attenuation.

There are several ways to achieve a phase shift using analogue circuitry. Many of the methods can be found in analogue audio processing effects, especially an *Audio Phase Shifter* (or simply a *Phaser*) which combines an audio signal with a duplicate which is modulated in and out of phase to create a subtle whooshing' sound [6, 7].

Reactive components can alter the phase of signals and by building networks of reactive components, the phase of the signal can be shifted. Below are two methods for achieving a variable analogue phase shift.

#### 2.4.1 All-Pass Filter

An all-pass filter shifts the phase of a signal while maintaining a constant gain throughout all frequencies. Figure 2.3 shows the schematic for an all-pass lead filter [14]. The output phase of the filter varies between  $180^\circ$  and  $0^\circ$  shown in Figure 2.4.

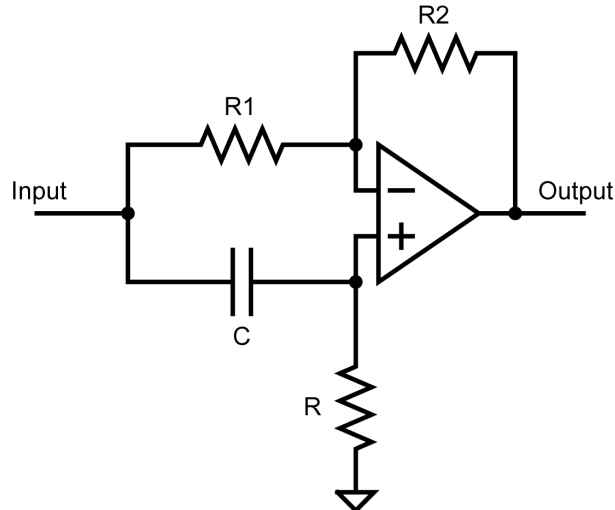


Figure 2.3: An Active First-Order All-Pass Filter. The output phase will lead the phase of the input.

The phase shift of a particular frequency  $f$  after passing through the filter is

$$\phi = 2 \arctan \left( \frac{f_0}{f} \right) \quad (2.3)$$

where

$$f_0 = \frac{1}{2\pi RC} \quad (2.4)$$

From (2.3) and (2.4) the phase shift of the cutoff frequency  $f_0$  can be calculated to be

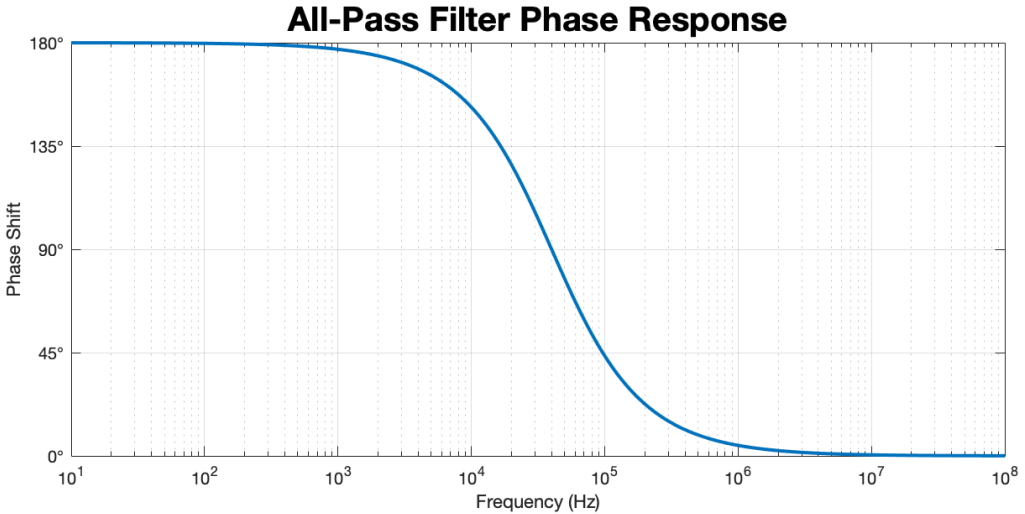


Figure 2.4: Phase Response of All-Pass Filter shown in Figure 2.3 where  $f_0 = 40\text{kHz}$

$90^\circ$ . This can also be seen in Figure 2.4.

By sweeping the resistance of  $R$  to a short circuit (and therefore shifting the cutoff frequency infinitely high), the phase of a sinusoid at the cutoff frequency is shifted from  $90^\circ$  to  $180^\circ$ .

This method of phase shifting is used in many audio phasers targeted towards guitar players, most notably, the *MXR Phase 90* which combines four of the all-pass filters as shown in Figure 2.3 in series. In order to alter the phase shift of the entire unit, the Phase 90 uses JFETs as variable resistors in parallel with the resistor  $R$ . By altering the voltage on the gates of the JFETs, the resistance of the JFETs is swept from, in the case of ideal components, an open circuit to a closed circuit. This is capable of shifting the phase of the cutoff frequency of each filter from  $90^\circ$  to  $180^\circ$  and therefore shifting the phase of the whole unit from  $0^\circ$  to  $360^\circ$  at the cutoff frequency [15].

#### 2.4.2 Analogue Delay

Since the source for the phase-shifters is a single sinusoid with a fixed frequency, any phase shift is equivalent to a delay in time and vice versa. This allows for the phase to be controlled by an analogue delay circuit.

As with the audio phasers discussed above, analogue delays are a common effect used in audio processing. The delaying of the signal within an analogue delay effect is often achieved using a chip known as a Bucket Brigade Devices (BBD) [3, 16]. A BBD consists

## CHAPTER 2. LITERATURE REVIEW & DEVELOPMENT OF THEORY

of a series of capacitors connected by gating transistors. By sequencing the opening of the transistors, an analogue signal can be 'sampled' into the first capacitor before being transferred down the series until it reaches the output. By controlling the rate at which the gating transistors are switched, the signal is delayed.

The drawbacks of BBDs are the losses as the signal is transferred between the capacitors as well as clock noise leaking into the signal [16]. Additionally, while the signal is never digitally sampled, the signal is still being sampled and thus must obey the Nyquist–Shannon sampling theorem. As the devices were designed for use with audio, they are optimised for a sampling rate of around 40kHz [3].

The most common BBDs are the Panasonic MN series [16]. The MN series consists of twelve chips which differ by the number of capacitor stages within. The most suitable devices for short delay times are the MN3012 and the MN3207 [3].

# **Chapter 3**

## **Subsystem Design, Testing & Integration**

Phased arrays are more versatile with as many units as possible, while this project only aims to test the system using four transducers, the project is designed to be as modular as possible and therefore infinitely scalable. This allows the full array to be expanded to a two-dimensional array - allowing for steering in the beam vertically as well as horizontally - using the existing modules with modified control circuitry.

The design of each module is detailed below.

### **3.1 Design of Phase Shifting Units**

As discussed above, each element of the array needs its own phase shifting unit. To have full control of the beam of the array, each phase-shifter should be able to shift from  $0^\circ$  to  $360^\circ$ . In order to keep control of the beam as simple as possible, the phase-shifter will be designed to shift according to a control voltage.

#### **3.1.1 Potential Solutions**

Based on these constraints, the following solutions were designed.

### Analogue Delay

As the entire array runs off a constant sinusoid, the phase shift can be achieved by delaying the signal. The ultrasonic transponders which were selected operate at 40kHz and the delay required to shift from 0° to 360° is equivalent to delaying by the period of the signal. The period of the signal and the required delay range is

$$T = \frac{1}{f} = \frac{1}{40\text{kHz}} = 25\mu\text{s} \quad (3.1)$$

As each transponder will have its own phase shifting unit, the phase shift (or in this case, the delay) does not necessarily need to be from 0° to 360°. As long as the phase shifting unit is able to provide a 360° shift, a constant offset will be consistent for all of the units and thus, with reference to the first unit, each unit can provide a 0° to 360° shift.

In order to achieve the delay, BBDs could be used. The Panasonic MN3012 has three parallel BBD delay lines capable of providing a 475μs to 9500μs delay. MN3012 can be clocked from 10kHz to 200kHz with the delay time inversely proportional to the clock frequency. This is seen in Figure 3.1 taken from the MN series datasheets [3].

### CLOCK FREQUENCY AND SIGNAL DELAY TIME

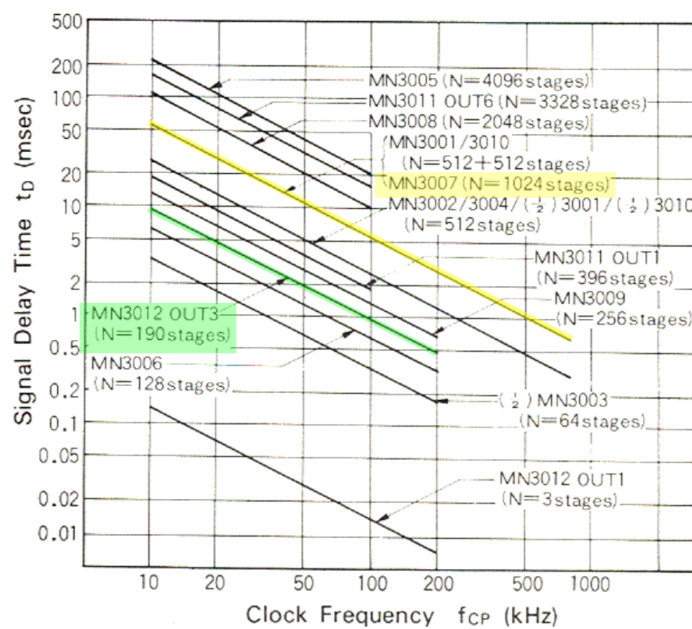


Figure 3.1: Clock Frequency vs Delay Time for the Panasonic MN series of BBDs taken from the datasheet [3]. The curves for the MN3012 and MN3007 have been highlighted in green and yellow respectively.

### 3.1. DESIGN OF PHASE SHIFTING UNITS

From this, a relationship of the clock frequency to the delay time can be determined as

$$f_{clock} = -(2.1053 * 10^7)t_{delay} + 210kHz \quad (3.2)$$

In order to satisfy the Nyquist–Shannon theorem, the clock frequency must always be greater than 80kHz. For this reason, the sampling frequency will be kept as high as possible. The delay will then be chosen to range from  $475\mu s$  to  $500\mu s$ . By plugging this into (3.2) the frequency range which the clock needs to sweep is from  $199.4735kHz$  to  $200kHz$ .

In theory this is a viable solution, however, the MN3012 has become almost obsolete and therefore the price per chip does not allow for a low-cost, infinitely scalable solution. The only readily available BBD currently is the MN3207, a low-current work-alike to the MN3007.

As with the MN3012, the required frequency range can be calculated from the curve shown in Figure 3.1. With a delay range from  $5120\mu s$  to  $5145\mu s$  the frequency range for the clock needs to be  $99.951kHz$  to  $100kHz$ . While this sweep is possible to generate, it is not practical as component tolerances become too significant. Additionally, the precision required for the clock frequency is not practical to be generated using analogue components and any digital solution would be more difficult than generating individual signals with the correct phase offset.

Based on this, it is believed that any sampled delay is not a practical solution for this project. While this report does not investigate the viability, this method may work using the Princeton Technology PT2399, a digital delay chip controlled by an external resistance [17].

### All-Pass Filter

In order to design a suitable all-pass filter, the phase shifting section of a *MXR Phase 90* was adapted for the operating frequency of  $40kHz$ . This is done by changing the values of the RC network shown in Figure 2.3 so that the cutoff frequency is  $40kHz$ .

$$f_0 = 40kHz = \frac{1}{2\pi RC} \quad (3.3)$$

The value of the capacitor was chosen to be  $47\text{pF}$  due to the ease of availability – a necessity whilst amidst the “global shortage” of ceramic capacitors [18]. Thus the value of R can be determined

$$R = \frac{1}{2\pi f_0 C} = \frac{1}{2\pi(40\text{kHz})(47\text{pF})} = 84.7\text{k}\Omega \approx 85\text{k}\Omega \quad (3.4)$$

Like the *MXR Phase 90*, the resistance of the RC network is altered using JFETs in parallel to the resistor. This is because JFETs can be used as a voltage-controlled resistor [19]

Each of the four stages is controlled by an independent JFET to shift the phase from  $90^\circ$  to  $180^\circ$ . In order to achieve the most linear response from the phase-shifting unit, each JFET needs to be ‘matched’ so that similar transistors are used. By matching the JFETs, the response of each stage is shifted by the same amount, minimising distortion and nonlinearities. The two important characteristics to match are the gate-source cutoff voltage  $V_{GS(off)}$  and the drain-source saturation current  $I_{DSS}$  [20]. As the characteristics of a batch of JFETs vary quite drastically, a large number of devices needs to be tested to find matched sets of four. Because of this, the J112 was selected as it was the most affordable to buy in bulk.

The schematic for the all-pass filter is shown in Figure 3.2. In order to shift the phase, the control voltage needs to be swept from ground to  $-V_{cc}$  as the resistance of the JFETs is decreased as the negative voltage increases.

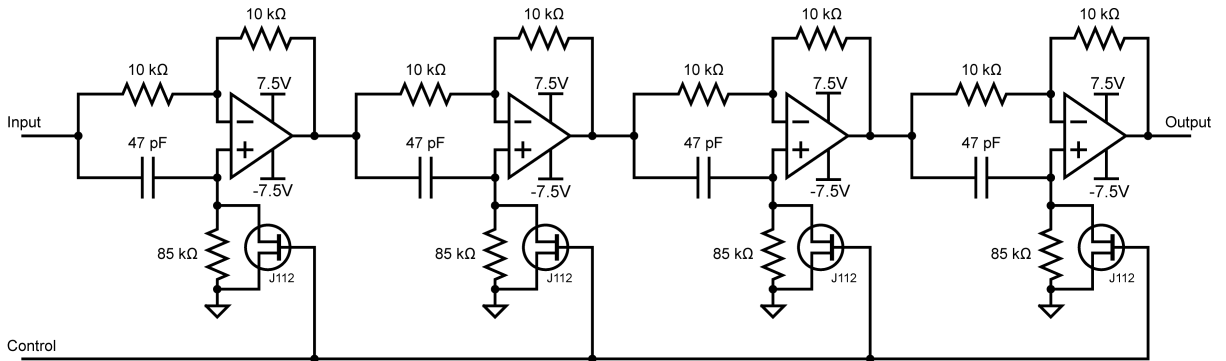


Figure 3.2: Schematic for All-Pass Filter capable of shifting a  $40\text{kHz}$  sinusoid from  $0^\circ$  to  $360^\circ$  based on the voltage of the control signal.

The schematic was simulated using LTSpice<sup>i</sup> to check the schematic before it is built. A screenshot of the LTSpice Model can be found in Appendix A. The schematic was simulated with the JFETs modelled as a short circuit and an open circuit to test the

<sup>i</sup>Analog Devices Inc. LTSpice XVII for OS X

### 3.1. DESIGN OF PHASE SHIFTING UNITS

extremes of the all-pass filters. The schematic was then simulated by sweeping the control voltage with the JFETs and observing the phase difference. The results of these simulations can be seen in Figures 3.3 – 3.5 below.

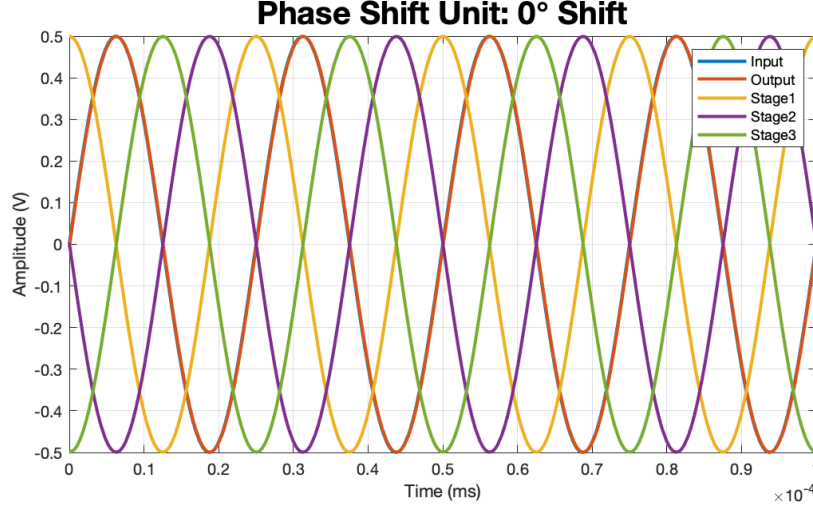


Figure 3.3: Simulated output for the phase shifting units shown in 3.2 with the JFETs modelled as an open circuit. The output can be seen to be in phase with and overlapping the input.



Figure 3.4: Simulated output for the phase shifting units shown in 3.2 with the JFETs modelled as a short circuit. The output can be seen to be  $360^\circ$  out of phase and overlapping the input.

Figures 3.3 and 3.4 show that the phase-shifting units are able to shift the phase a full  $360^\circ$  out of phase. This allows full flexibility of the phase shifting units. Figure 3.5 shows the full phase shifting capabilities when controlled by the JFETs. The control voltage or  $V_{GS}$  range of interest is from  $-2V$  to  $-3V$ . While the signal is shifted completely, there is both signal attenuation as well as a DC offset introduced as the signal transitions.

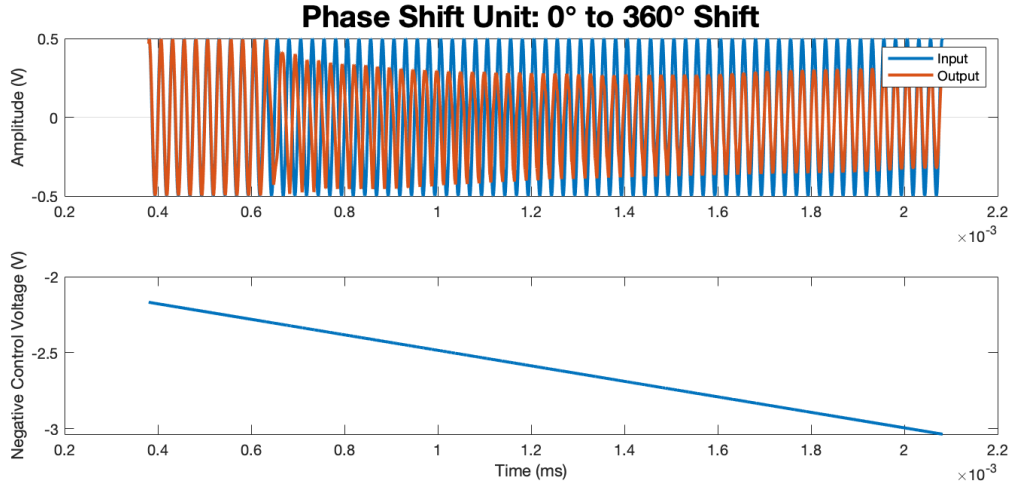


Figure 3.5: Simulated output for the phase shifting units shown in 3.2 with the control voltage swept from  $-2V$  to  $-3V$ . The output can be seen shifting from  $0^\circ$  to  $360^\circ$ . Additionally, some attenuation to the signal as well as a DC offset can be observed as the signal transitions.

The signal attenuation is as a result of the drain-gate current which flows through the JFETs. The output of each of the opamps is given by

$$V_{out} = -V_{in} + 2V_0 \quad (3.5)$$

where  $V_0$  is the voltage at the inputs [15]. Since there is a negative feedback loop in the opamp circuit, each of the two inputs are, in an ideal case, equal. Thus,  $V_0$  can be viewed as the output of the voltage divider created by the capacitor, resistor and JFET. A simplified form of this is shown in Figure 3.6 below. The reason behind the

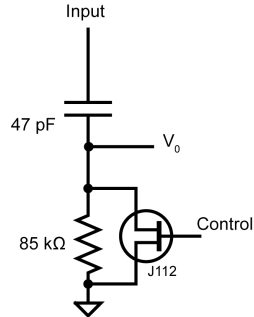


Figure 3.6: Isolated voltage divider

attenuation when the JFET is added is due to current being lost through the gate of the JFET. Kirchhoff's Current Law (KCL) states that the net current at any node is zero. Thus, any current that flows out of the gate of the JFET means that less current flows through the resistor. This, in turn, means that the potential across the resistor is less which decreases  $V_0$ . This is propagated through each of the four stages which attenuates

### 3.1. DESIGN OF PHASE SHIFTING UNITS

the signal.

The DC offset only occurs as the effective resistance changes. For the positive half of the input wave, as the resistance decreases, the voltage at the non-inverting inputs of the opamps is decreased as it approaches ground. Because of the negative feedback loops, the voltage at the inverting input also decreases causing more current to flow from the input through the resistor to the inverting input. As the input impedance of the opamps is theoretically infinite, this greater current flows through the feedback resistor lowering the output voltage. Applying the same principals, the output of the negative half of the waveform can also be shown to also be lower. Without the capacitors, the voltage at the non-inverting would simply be at ground potential as, in theory, no current would flow through the resistors. Additionally, with a fixed resistance, the capacitor charges and no current flows through. Thus the DC offset only occurs as the resistance changes.

By sweeping the control voltage over a longer time period to fit more periods within the phase-shifting region, the relation of phase shift to control voltage was plotted. To plot the relationship, the data from LTSpice was analysed and plotted using MATLAB<sup>ii</sup>. This can be seen in Figure 3.7 below.

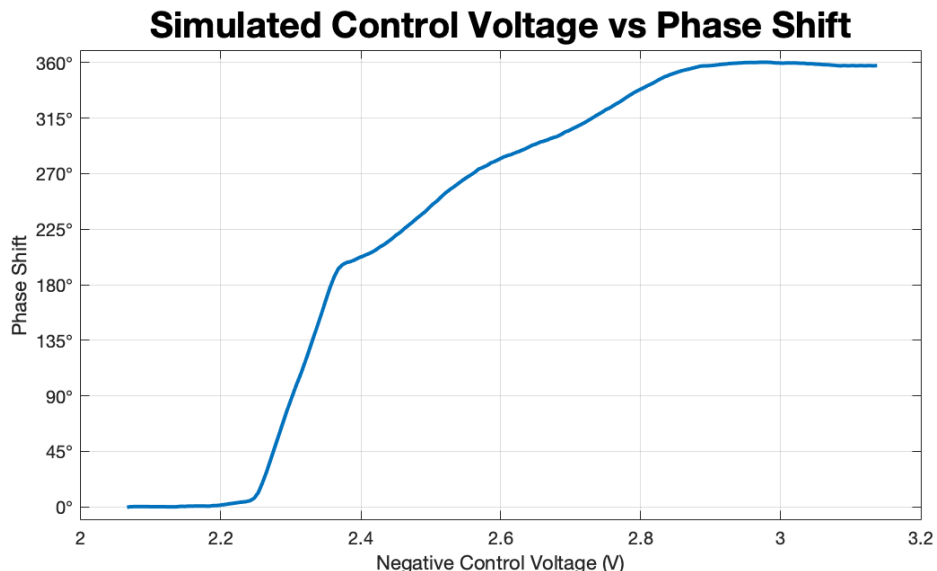


Figure 3.7: Simulated relationship between control voltage and phase shift. The curve can be seen to have two roughly linear regions.

The relationship between the control voltage and the phase shift can be seen to have two roughly linear regions. The first is as the JFETs transition from their on-state to the linear region and the second is the linear region and the transition to the off-state.

---

<sup>ii</sup>MathWorks MATLAB R2018a 9.4.0.813654 for OS X

Despite the attenuation and offset, the simulations show the all-pass filter as a phase-shifter as a viable solution as it meets the desired specifications of the full  $360^\circ$  phase-shifting shifted by a control voltage. In addition to this, the parts required for construction are all inexpensive and readily available.

### 3.1.2 Circuit Design & Testing

The schematic for the all-pass filter shown in Figure 3.2 has been shown to work in simulation and so the next logical step is to physically test the circuit. This was first done by constructing the schematic on a breadboard and addressing any issues before retesting and designing a PCB layout.

#### Breadboard design

Before the schematic was constructed, a set of matched JFETs was needed. In order to measure the gate-source cutoff voltage  $V_{GS(off)}$  and the drain-source saturation current  $I_{DSS}$ , an Arduino-based measurement box was constructed based on a schematic designed by runoffgroove.com [21]. This can be found in Appendix C. Once a set of JFETs had been found, the schematic was built on a breadboard using LM741 opamps. As the tolerance of ceramic capacitors is usually quite low, the resistors in the RC network were replaced with a multi-turn  $100k\Omega$  trimmer pots. This allows the RC networks to be fine-tuned in order to set the phase shift of each unit to be as close to  $90^\circ$  as possible. The breadboard layout can be found in Appendix B.

Once the layout had been built, the circuit was powered and a  $40\text{kHz } 1V_{pp}$  sine wave was supplied to the input. The control voltage was set to the  $-7.5V$  in order to calibrate the  $360^\circ$  phase shift using the trimmer pots. Upon testing, it was noticed that each stage was loading the previous stage causing signal distortion. In order to prevent this, a non-inverting opamp buffer was added between each stage. The full revised schematic can be found in Appendix B. With the addition of the buffers, the output of each stage was tuned to provide a  $360^\circ$  phase shift at the output. By varying the control voltage, the output phase was seen to shift from  $0^\circ$  to  $360^\circ$ . As this is a proof of concept for the circuit, a more permanent circuit was constructed.

### 3.1. DESIGN OF PHASE SHIFTING UNITS

#### Veroboard & PCB Design

The schematic was designed as a PCB layout using Altium Designer <sup>iii</sup> before being sent off to be fabricated. In order to reduce cost and physical size, the eight LM741 opamps were replaced with two LM324N quad opamps. While the PCBs were being fabricated, a layout of the circuit was constructed on veroboard in order to test the driver circuitry for the transducers as discussed below. These layouts can be found in Appendix B.

Using a  $1M\Omega$  trimmer pot to set the control voltage, the PCB phase-shifters were tested by measuring the phase shift with an oscilloscope. The results of this can be seen in Figure 3.8 below.

The acquisition of the control voltage and phase shift relation was fairly difficult to measure. This test was performed by triggering a single trigger from the oscilloscope and manually sweeping across the voltage range. This test was repeated for each of the phase shifters which are expected to have different results due to the differing pinch voltages of the JFETs. The tests required significant interpolation as the recorded data from the oscilloscope was noticeably discrete.

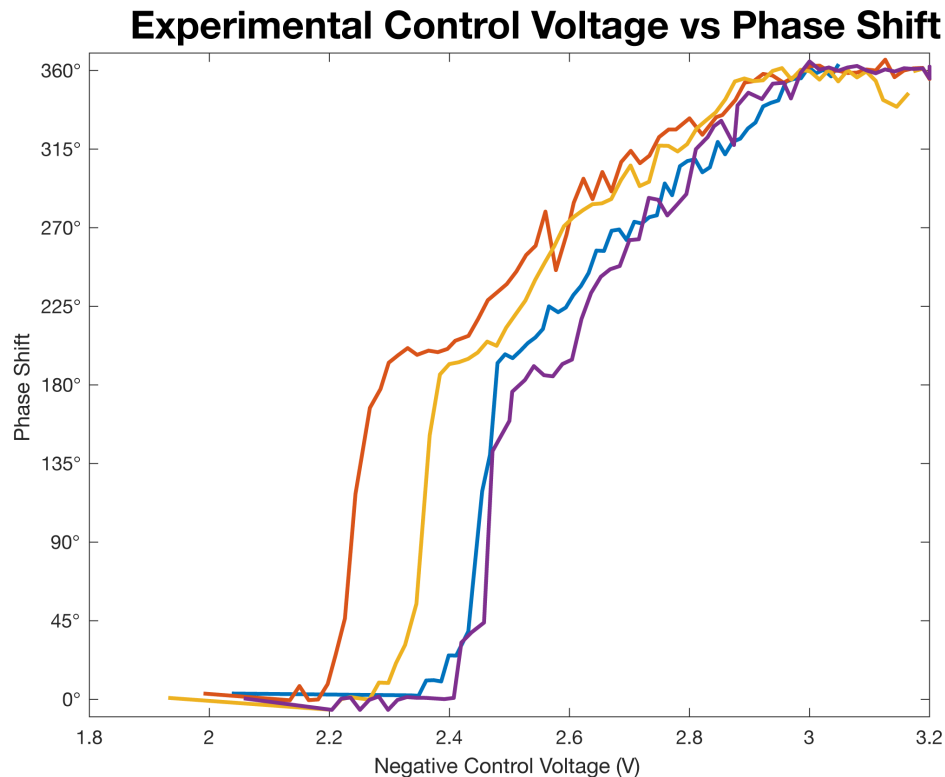


Figure 3.8: Tested relationship between control voltage and phase shift

---

<sup>iii</sup>Altium Designer 17.1 for Windows 10

### CHAPTER 3. SUBSYSTEM DESIGN, TESTING & INTEGRATION

The tested results of the phase shift units showing a full  $360^\circ$  of phase shifting. The results show that the different JFETs have a noticeable impact on the phase response despite all of the JFETs being chosen to have a pinch voltage as close to 3V as possible. With the use of a multi-turn trimmer pot setting the control voltage the phase shift could be set to any position, however, as seen by the graphs this is very susceptible to noise.

Due to the inconsistencies with JFETs, these results were not compared with the simulated results directly. Any direct calculation of a mean squared error (MSE) leads to a significant error as a result of the curves not lining up despite the close resemblance of the graphs. In addition to this, the characteristics of the SPICE model likely do not align with any of the sets of 4 matched JFETs. While this is a rather undesirable result, as mentioned above, attempts to manually set the phase shift proved possible with the use of a multi-turn trimmer. This allowed for the phase shifters to be used in order to test the rest of the array. Possible improvements to this design are discussed in the Recommendations at the end of the report.

As with the simulated results, the signal is attenuated as the phase shift is increased. While this is not an ideal case, due to the nature of the ultrasonic transponders, this will not be an issue as explained in the next section of the report.

## 3.2 Design of Transducer Driver Circuits

The transducers selected for this project, the Mobicon UT1612MPR [8], were selected as they were the only transponders available within the budget constraints of the project. The transducers are available at 40kHz and 25kHz. Despite the limitations that only choices of transducer affords, the scope of this project is to test a proof-of-concept and, if successful, the concepts can be applied to more expensive transducers. As discussed in the previous chapter, higher frequencies are preferable for phased arrays and many more expensive transducers operate at 40kHz and so to allow for as much growth as possible, the 40kHz transducers were selected.

### 3.2.1 Requirements of Transducer Driver Circuits

The datasheet for the Mobicon UT1612MPR provides little information on how to power the transducers apart from specifying a frequency tolerance of  $40\text{kHz} \pm 1\text{kHz}$  and the maximum input voltage of  $20V_{pp}$  [8]. As the only electrical characteristic specified is a capacitance, it was assumed and later confirmed by testing, that the transducers were piezoelectric and are designed to be powered with a square wave rather than a sinusoid like a speaker would require.

The above requirements show that the driver circuitry needs to take the sine wave which is outputted from the phase shifters and output a square wave of the same frequency and phase. The amplitude of this square wave was chosen to be  $15V_{pp}$ . This value was chosen as the datasheet only specifies that  $20V_{pp}$  is the maximum voltage, however, it does not specify whether this is an absolute maximum or an operating maximum. A value of  $15V_{pp}$  should be suitably high enough for testing without potentially damaging the transducers.

### 3.2.2 Theory & Simulations

In order to convert the sine wave to a square wave, the signal needs to be fed through a comparator. The output of the desired comparator can be given by

$$V_{out} = \begin{cases} 7.5V & x \geq 0 \\ -7.5 & x < 0 \end{cases} \quad (3.6)$$

This equation is unaffected by the amplitude of the input sinusoid which compensates for any attenuation caused by the phase-shifters.

A standard opamp can be used as a comparator however, most affordable opamps, such as those used in the phase-shifting circuits, are not designed to switch at 40kHz. Figure 3.9 shows that the slew rate of the LM741 becomes significant causing the output wave to become rounded and that the output does not swing all the way to the rails. Perhaps the most notable trait is that the phase of the square wave output is not the same as the phase of the sine wave input. Screenshots of the simulated LTSpice schematics for all of the circuits can be found in Appendix A.

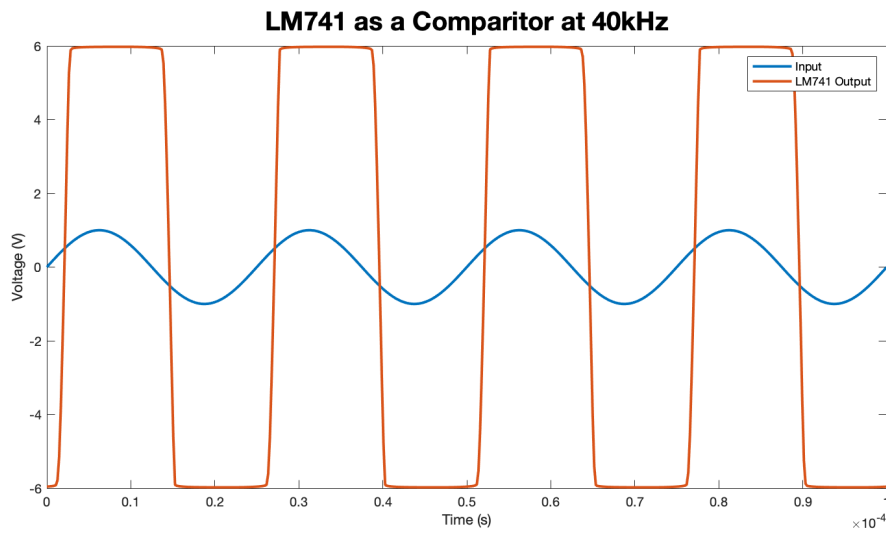


Figure 3.9: Simulated output of an LM741 used as a comparator at 40kHz

Part of the reason for the effect of the slew rate is that the opamp is switching from rail to rail. In order to rectify this, a comparator IC such as the LM311 can be used. The LM311 has a BJT on the output of the comparator section which reduces the need for the opamp section to swing to the rails as it only needs to switch the base of the BJT. The topology of the LM311 can be seen in Figure 3.10 below taken from the LM311 datasheet [4].

By using the LM311, all of the above issues are addressed. Figure 3.11 shows the response of both the LM741 opamp as well as the LM311 comparator.

Figure 3.11 shows that the LM311 is a far superior device for this application. as the output is exactly as desired. However, the simulation shows the output without any load. The datasheet for the transducer shows that the device has a capacitance of around 2000pF. Figure 3.13 shows the loaded output of the comparator. In order to reduce the

### 3.2. DESIGN OF TRANSDUCER DRIVER CIRCUITS

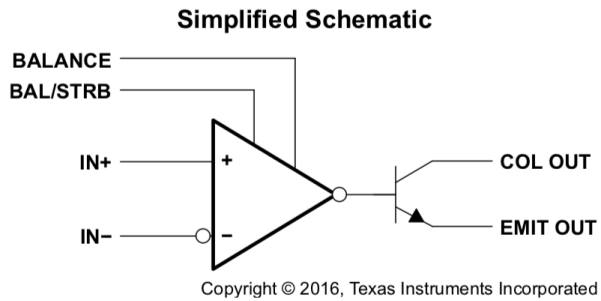


Figure 3.10: LM311 internal topology showing BJT output stage. Image taken from LM311 datasheet [4].

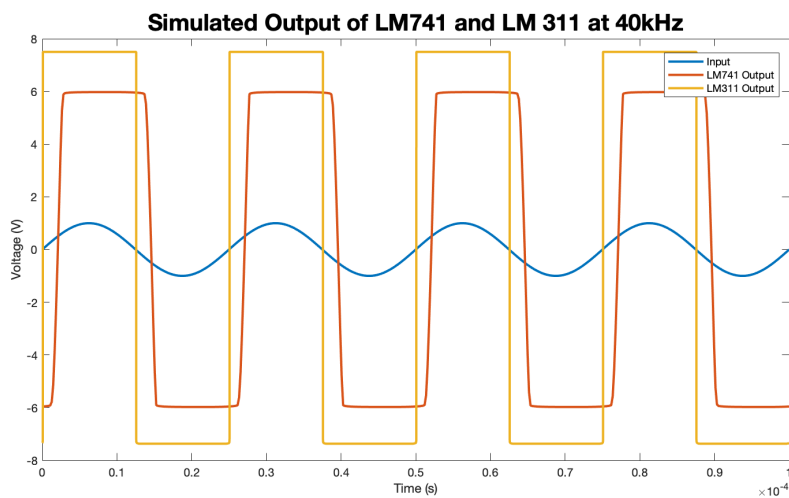


Figure 3.11: Simulated output of LM741 used as a comparator as well as the LM311 at 40kHz.

loading, a buffer is needed. For similar reasons to an opamp not working above, opamp based buffers suffer from slew rate issues. A slightly unconventional approach to buffering is to use a buffered inverter such as the CD4069 Hex Inverter [22]. The CD4069 requires no external parts and is able to buffer the signal without significant loading. The inverter, obviously, does invert the signal, however this can be compensated for by switching the inputs of the comparator. Figure 3.14 below shows the simulated output of the whole transducer driver circuitry, while Figure 3.12 shows the final schematic.

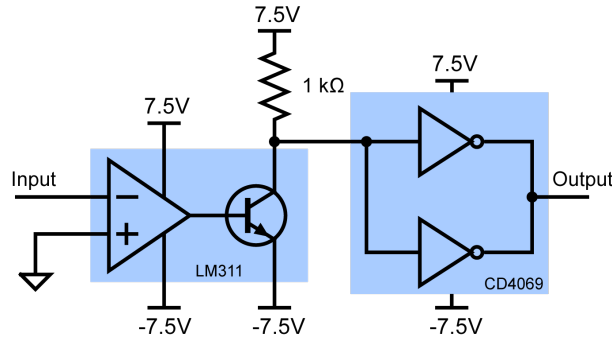


Figure 3.12: Schematic for transducer driver circuitry

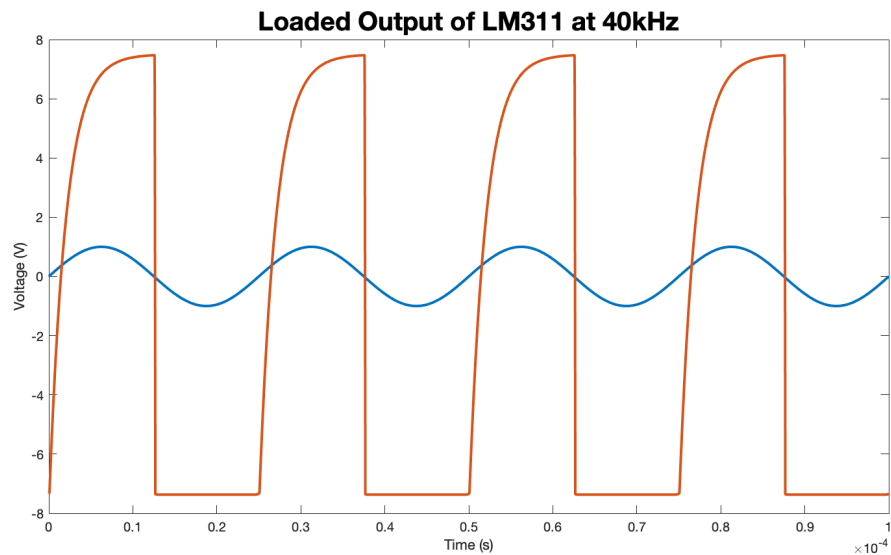


Figure 3.13: Simulated output of LM311 at 40kHz with 2000pF load.

### 3.2. DESIGN OF TRANSDUCER DRIVER CIRCUITS

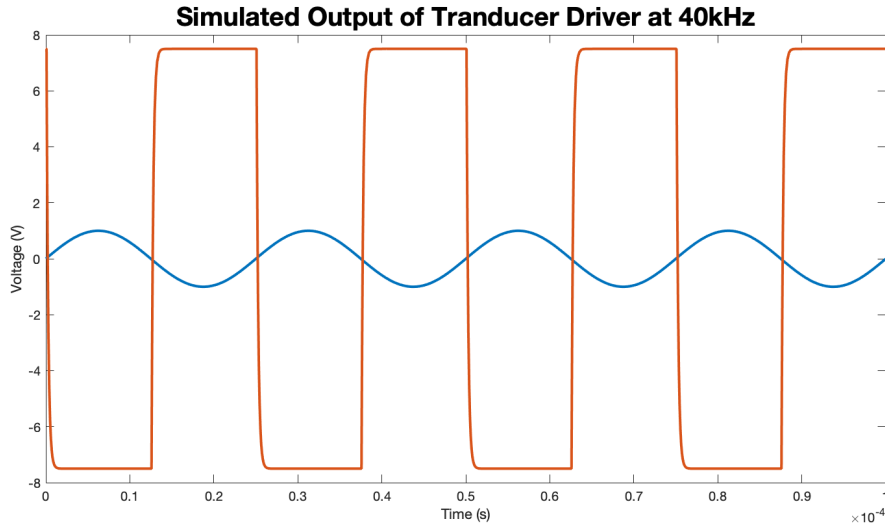


Figure 3.14: Simulated output transducer driver with load

#### 3.2.3 Breadboard & Veroboard Design

The schematic as seen in Figure 3.12 was tested on a breadboard before being constructed on veroboard both of which can be seen in Appendix B. Due to time constraints, the schematic was not fabricated as a PCB.

By running the transducer driver off the output of one of the phase-shifting units, the veroboard circuits were tested. The results of this test can be seen in Figures 3.15 and 3.16 below. In order to test that the transducer was indeed outputting, an ultrasonic receiver was measured using an oscilloscope and placed in front of the transducer. The oscilloscope showed that the receiver was receiving a 40kHz sinusoid, confirming that the driver circuitry works.

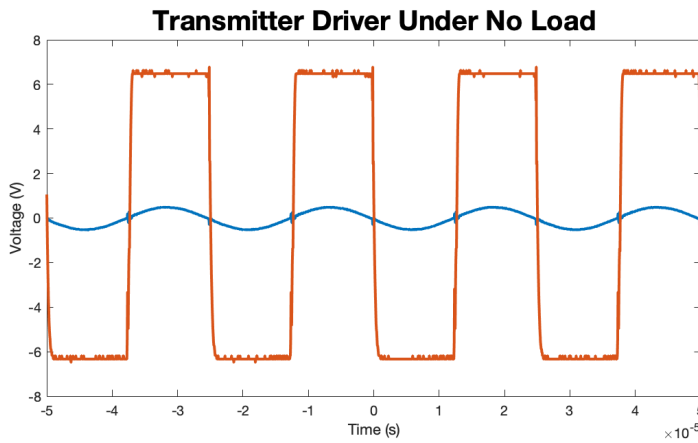


Figure 3.15: Experimental output of transducer driver without load

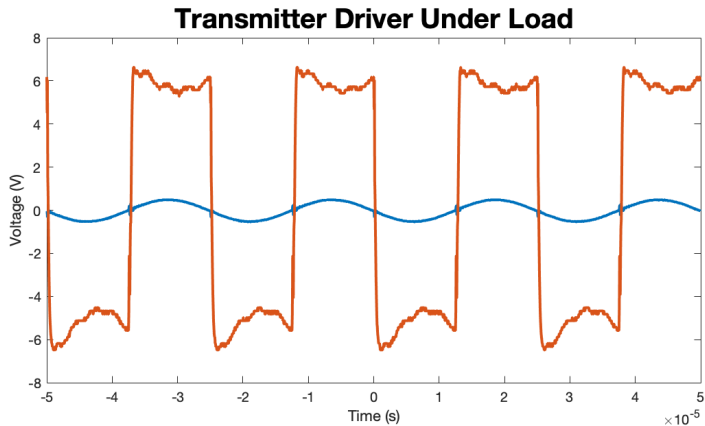


Figure 3.16: Experimental output of transducer driver with load

The results seen in Figures 3.15 and 3.16 show that the driver works perfectly under no load but experiences loading with the transducer. The nature of this loading does not resemble that of the unbuffered output as shown in Figure 3.13. The output is still relatively square.

## 3.3 Beamforming

Beamformation is the process by which the outputted wave of the entire array is designed. Through the constructive and destructive interference of the audio waves, the full spread of each element of the beam can be narrowed down to a single steerable beam [1].

### 3.3.1 Beamforming with Ideal Transducers

As discussed in the literature review, in order to achieve a single beam out of the antenna, each element in the array needs to be placed half a wavelength away from the adjacent elements. The wavelength of a signal is given by

$$\lambda = \frac{v}{f} \quad (3.7)$$

where in this case,  $v = 343\text{m/s}$ , the speed of sound in  $20^\circ\text{C}$  air, and  $f = 40\text{kHz}$ . This gives

$$\lambda = \frac{343}{40000} = 8.575\text{mm} \quad (3.8)$$

Thus the ideal positioning of the ultrasonic transducers is with  $4.29\text{mm}$  between their centres. This was simulated using MATLAB to show the simulated output of the array. An array of four elements all in phase with each other was simulated to show the beamshape with  $\frac{\lambda}{2}$ ,  $\lambda$  and  $2\lambda$  spacing between elements. The results of these simulations are shown in Figure 3.17 and the MATLAB code can be found in Appendix D.

### 3.3.2 Beamforming with Non-Ideal Transducers

The physical size of the transducers is around  $16.2\text{mm}$  [8]. This is roughly twice the wavelength meaning that the output of the array is expected to have large grating lobes. These simulations assume that the transducers have a  $180^\circ$  beam angle, however, the datasheet for the transducer specifies a maximum beam angle of  $80^\circ$  [8]. This means that the transducers cannot create the grating lobes which are perpendicular to the main beam as they are outside the throw of the transducer. However, the lobes at  $60^\circ$  and  $120^\circ$  will still be formed.

In order to stop these grating lobes from forming, the transducers were removed from their aluminium casings and the housings modified to allow them to be placed as close as

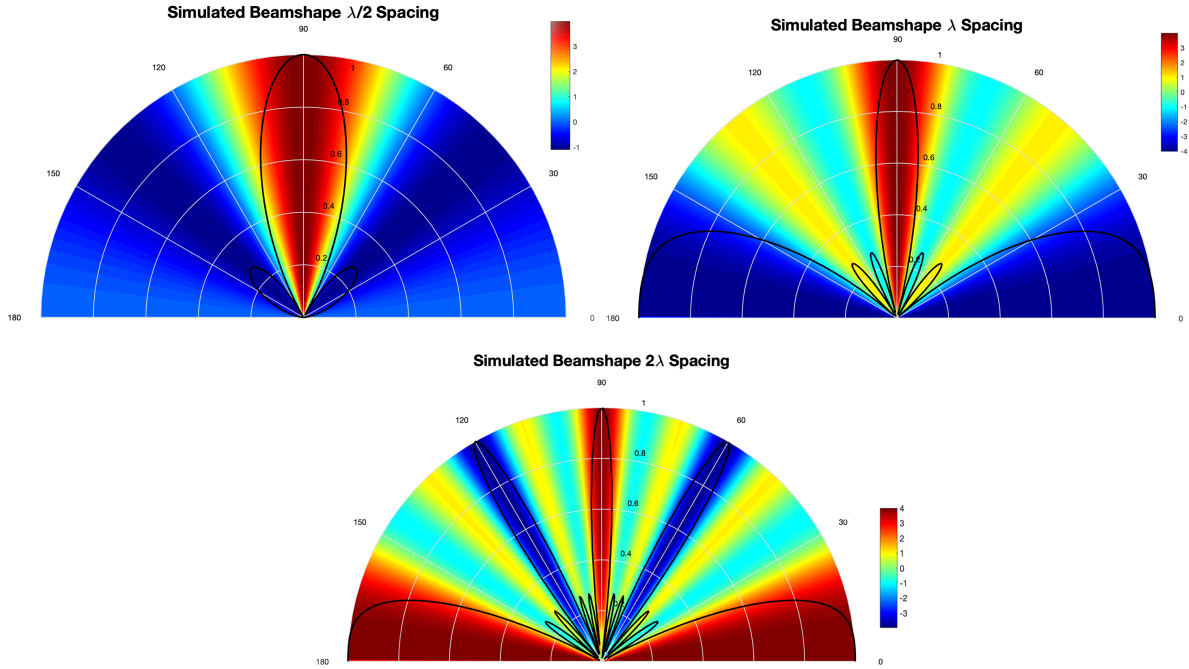


Figure 3.17: Simulated beamshape of four in-phase elements with  $\frac{\lambda}{2}$ ,  $\lambda$  and  $2\lambda$  spacing. Note that for the  $\frac{\lambda}{2}$  case the grating lobes are roughly a quarter the amplitude of the main beam while in the other two cases the grating lobes are the same amplitude as the main beam. Additionally, the number of grating lobes roughly doubles as the spacing does.

physically possible. The modified transducers have a width of 9.75mm as seen in Figure 3.18. This is significantly closer to a single wavelength.

Before all of the transducers were deconstructed, the modified transducer was tested against an unmodified one. The results of this can be seen in Figure 3.19 which shows the addition of small grating lobes and attenuation of amplitude, however, the results show that the implications of the modified transducers are relatively minor compared to that of unmodified spacing the transducers.

The array was again simulated while taking into account the beam angle of the transducers and the revised spacing. Figure 3.20 shows the simulated output of the four modified transducers in-phase with each other. The simulated array can be seen to produce a single main beam with relatively small grating lobes. The graph also shows the expected output of a transducer with an omnidirectional beam showing that while large grating lobes are expected, the limited beam angle of the transducer does not allow for them to form.



Figure 3.18: Measured size of unmodified and modified transducer

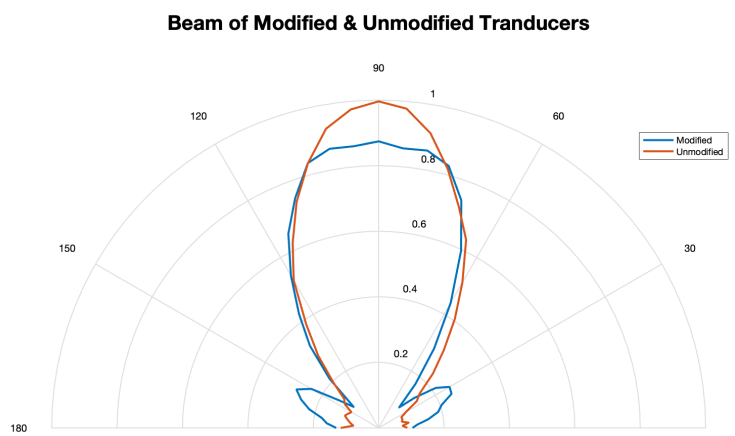


Figure 3.19: Beam of modified and modified transducers. The modifications to the transducer result in added grating lobes and attenuation.

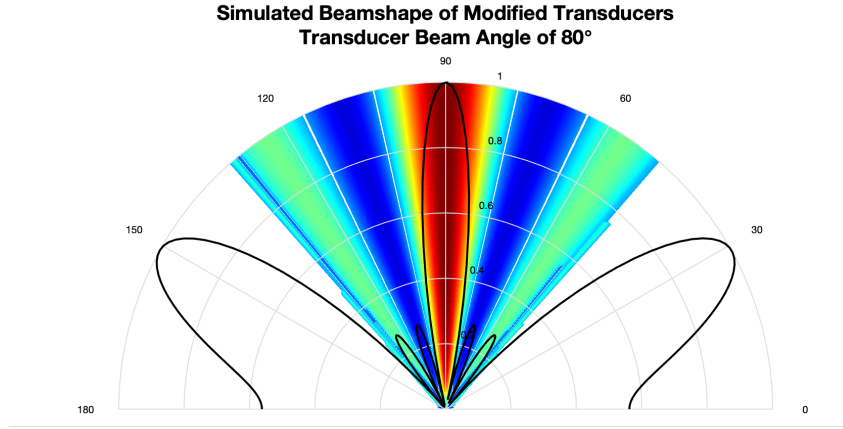


Figure 3.20: Simulated Beam of four modified transducers. The simulation shows a single main beam with small grating lobes. The black trace shows the response of omnidirectional transducers showing the beam angle prevents the formation of the large grating lobes.

## 3.4 Integration of Subsections

This section has shown each of the subsections to work in isolation and simulation, however, each of the subsections need to be combined to build the complete array.

There are two configurations in which the subsystems can be combined. Each system has strengths and weaknesses as discussed below.

### Configuration 1

The first configuration as seen in Figure 3.21 has each phase-shifter supplied with the same input waveform and a separate control voltage for each phase shifter. This allows the phase of each unit to be shifted to any phase shift. Each phase-shifter is then fed into a driver circuit before powering the transducer.

The individual control of phase shift allows the beam to be steered in either direction as well as, when more array elements are present, the beam to be split into multiple beams. The drawback of the configuration is that there are as many control voltages needed as elements in the array limiting the scalability of the array.

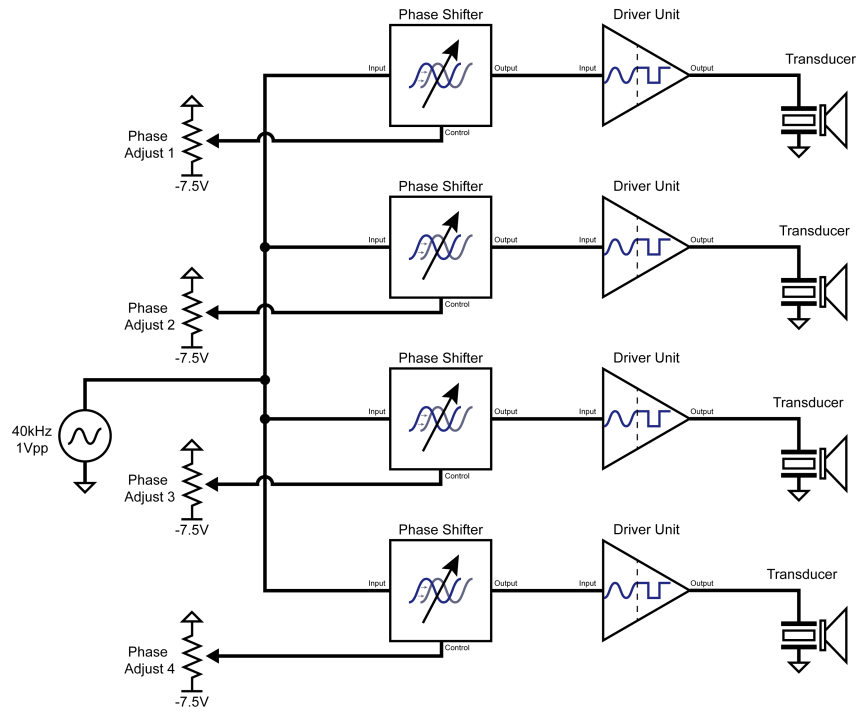


Figure 3.21: Possible configuration 1

## Configuration 2

The second configuration as seen in Figure 3.22 has the input waveform fed into a single phase-shifter and the subsequent phase-shifters fed off of the previous output. The control voltage for each phase-shifter is the same. This means that each phase-shifter is cascaded allowing a single control voltage to steer the beam. This configuration allows for infinite scaling in multiple dimensions while retaining a single control voltage however, the beam cannot be split into multiple beams and the control voltage can only introduce a positive phase shift. While the beam can still be steered to any possible position, it cannot be steered from across the  $0^\circ$  point. Additionally, each phase-shifter needs to respond to the same control voltage in the same manner, this requires every phase shifter's JFETs to be matched to the same values.

For the testing of this project, configuration 1 was selected. This is due to both the difficulty of finding 16 matched JFETs as well as added finer control over the phase shift of each element.

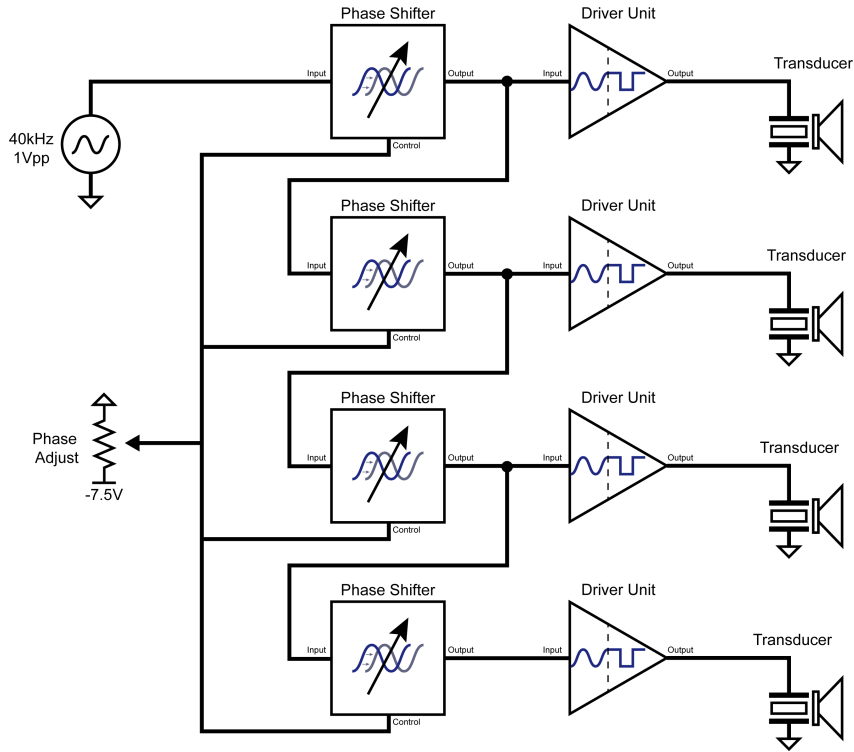


Figure 3.22: Possible configuration 2

### 3.5 Test Rig & Procedure

In order to test the steering capabilities of the array, a single receiver transducer was setup approximately two meters away from the transducer array. The array was then placed on a rotating platform. By rotating the platform beginning with the array pointing perpendicularly to the receiver, through  $180^\circ$ , the shape of the beam can be plotted. The rotating platform was laser cut out of hardboard allowing for a step size of  $5^\circ$  and, for a sweep through  $180^\circ$ , 37 data points. The array on its rotating platform can be seen in Figure 3.23 and the laser cutting template can be found in Appendix C.

All of the circuitry was powered with a  $\pm 7V$  power supply from which 148 mA was drawn. The inputted waveform was supplied from a function generator set to output a  $1V_{pp}$  sinusoid at 40kHz. Each output of the four phase-shifters was scoped on a single 4-channel oscilloscope in order to set and measure the phase shift.

The receiver was measured with a second oscilloscope with an external trigger fed from the function generator. This external trigger prevents the oscilloscope from triggering on noise. In order to record the amplitude of the received signal, the measured waveform on the oscilloscope was saved to a CSV file allowing for external data processing.

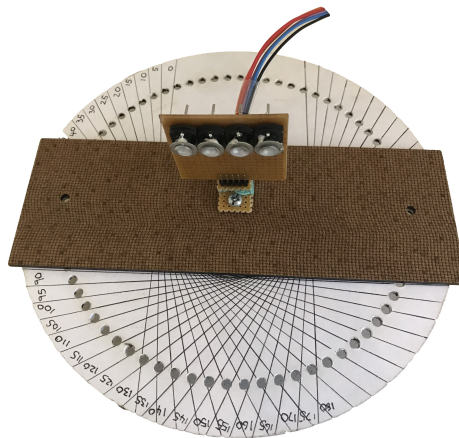


Figure 3.23: Transducer array mounted onto the rotating platform allowing

The CSV data can be analysed in using three methods outlined below.

1. Peak-to-Peak measurement. The amplitude is calculated by adding the maximum and minimum values of the data. This is not a reliable method as any noise spike or noise with higher amplitude than the measured sinusoid will lead to incorrect data.
2. RMS measurement. The RMS of a signal is proportional to the square root of the power through a fixed resistance. Any noise spikes have comparatively little power to that of the main waveform providing a more accurate result. The RMS value can then be scaled to find the peak voltage and doubled to find the amplitude. While better than the peak-to-peak measurement, this method will result in an offset as a result of the average power of the noise.
3. Fourier Transform measurement. Assuming the output is exclusively at 40kHz and that the noise at 40kHz is negligible compared to the measured signal, a discrete Fourier Transform of the data can be taken and the amplitude of the 40kHz component can be calculated. While requiring more processing, this is clearly the most accurate method of determining the received amplitude as it is able to ignore any irrelevant data.

The decision was made to use the Fourier Transform to collect the amplitudes to completely ignore the effects of noise. The amplitude at each angle can then be plotted on a set of polar axes to view and compare the beamshapes.

# Chapter 4

## Results

### 4.1 Simulation Results

Before the array was tested, the tests were simulated to provide an expected output which the measured data can be compared. The expected output at each stage is calculated using the equation of a wave

$$y(r, t) = A \cos(2\pi f_0 t + kr + \phi) \quad (4.1)$$

where  $r$  is the distance from the transmitter,  $f_0$  is the frequency,  $k = \frac{2\pi}{\lambda}$  and  $\phi$  is the phase shift. Substituting in for  $k$  and fixing the time gives

$$y(r, 1) = A \cos\left(2\pi f_0 + \frac{2\pi}{\lambda} r + \phi\right) \quad (4.2)$$

By summing the outputs of each transducer to simulate a 2-meter distance between the array and the receiver, the expected beamshape can be simulated. As this theory for a phased array applies to an omnidirectional transmitter, in order to simulate the effects of the modified transducers, the calculated output at every value of  $\theta$  was multiplied by the corresponding magnitude as shown in Figure 3.19.

For easy comparison, the test was simulated with both a continuous  $\theta$  as well as a discretised  $\theta$  to compare to the discrete results.

This can be seen in Figure 4.1 below. The individual graphs can be found in Appendix C.

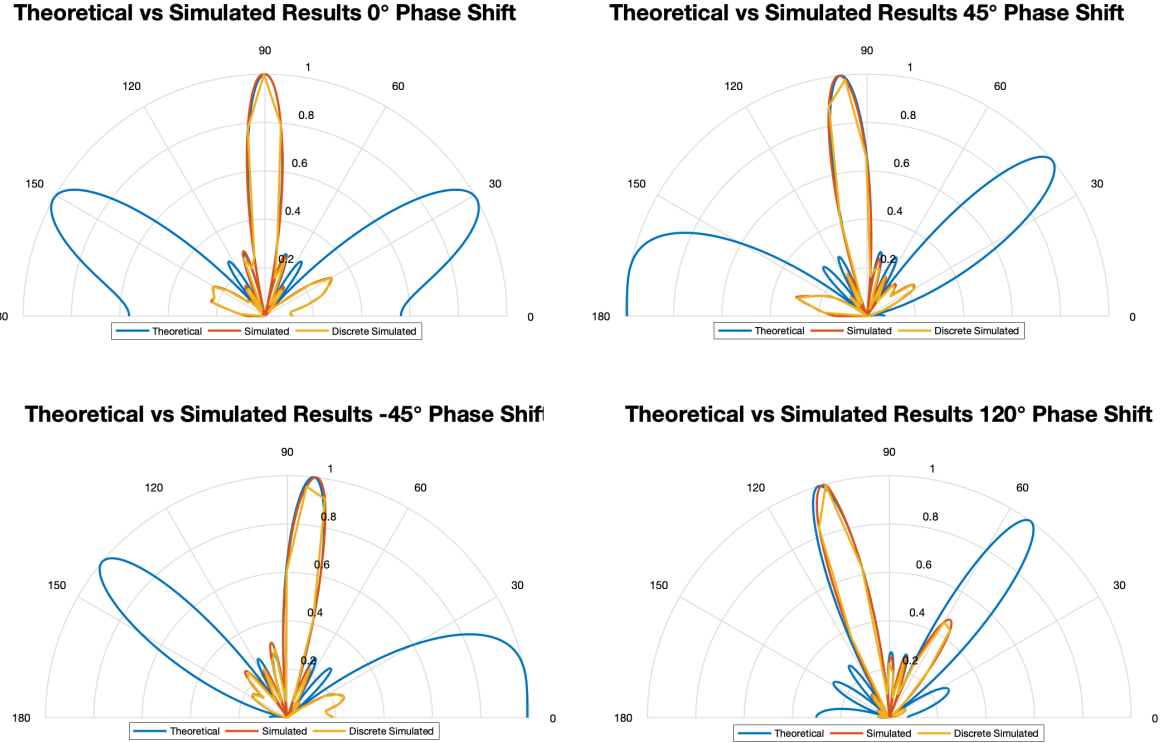


Figure 4.1: Simulated and theoretical results of the array

For the simulation, four test cases were simulated  $0^\circ$ ,  $45^\circ$ ,  $-45^\circ$  and  $120^\circ$ . These values were chosen to show that the beam can be steered in both directions as well as steered a somewhat significant amount.

## 4.2 Experimental Results

As with the simulated results, the array was tested with a relative phase between each unit of  $0^\circ$ ,  $45^\circ$ ,  $-45^\circ$  and  $120^\circ$ .

Each test provides 37 amplitude readings for a  $180^\circ$  sweep in  $5^\circ$  increments. Each test was repeated three times in order to provide a more reliable average beamshape. Because of this, the results are only able to show the angle of the steered beam to be an increment of  $5^\circ$ . While this limits the precision of the results, the tests are still able to show the steering capabilities.

As discussed above, the amplitude readings were taken by measuring the receiver with an oscilloscope and saving a CSV file of the measured waveform. The signal for each

## CHAPTER 4. RESULTS

measurement was then Fourier Transformed using MATLAB's Fast Fourier Transform (FFT) function to obtain the measured amplitude of the signal. Figure 4.2 shows an example of two measured waveforms containing significant noise and their FFTs. From this it can be seen that the noise in each case is fairly consistent for each measured waveform while there is a significant change in the 40kHz component.

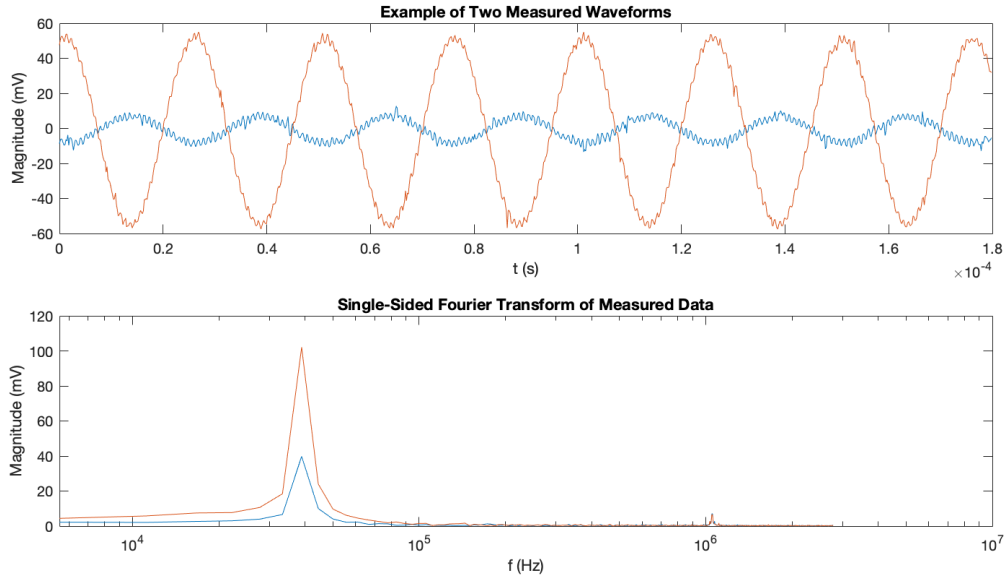


Figure 4.2: Example of measured data and corresponding Fourier Transform

The results of the four sets of measurements can be seen in Figure 4.3. This figure is intended to show the difference between the four tests, the individual figures can be found in the discussion section of the report below. To make the plots clearer, the individual test data has been lightened while the average beamshape in each case has been darkened. As with the simulated results above, each of these graphs can be found in Appendix C for a more detailed view.

The results of the experiments show the beam being shifted in the expected directions. The beam in each case can be seen to have a single main lobe with small grating lobes in the extreme angles. These results are further analysed and compared to the simulated results in the discussion below.

## 4.2. EXPERIMENTAL RESULTS

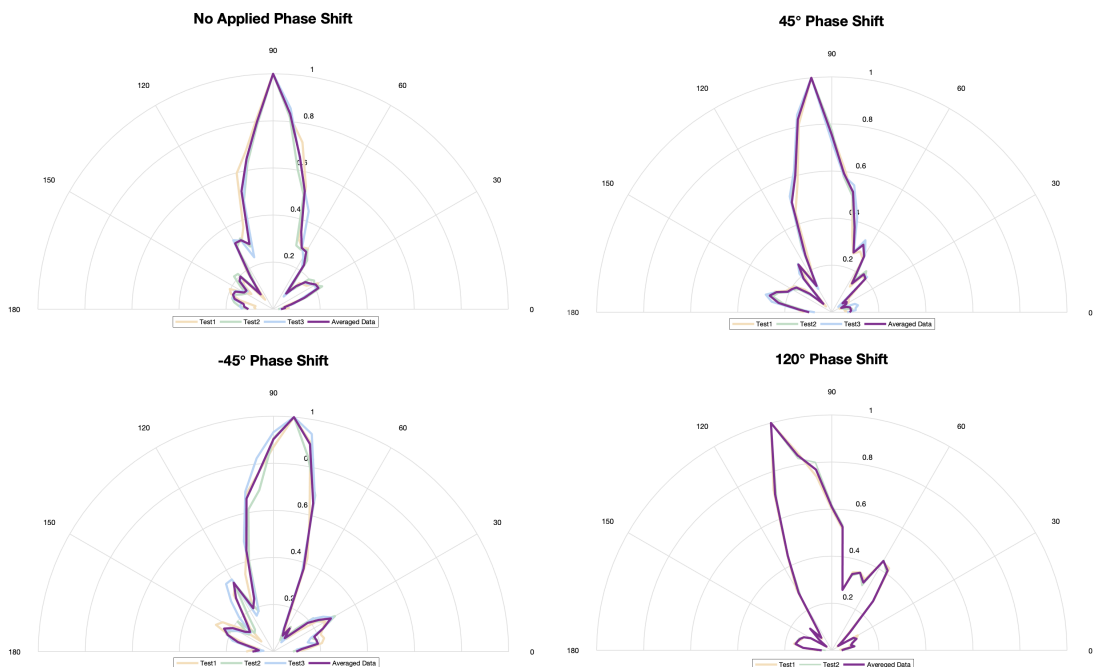


Figure 4.3: Transducer array mounted onto the rotating platform allowing a  $180^\circ$  sweep in  $5^\circ$  increments

# Chapter 5

## Discussion

In order to fully test the performance of the array, the experimental results are compared to that of the simulated results. However, before this is done, the simulated results are compared to the expected results as predicted by the theory. This will confirm the accuracy of the simulations and ensure that the modifications to the transducers do not have an effect on the main lobe of the beam. Once the validity of the simulations has been confirmed, the experimental results can then be compared to the simulations to provide insight into the performance of the array.

### 5.1 Simulated Results Compared to Theory

As discussed before and shown in (2.2) above, the theoretical beam angle for a linear phased array can be found as a function of the relative phase shift.

$$\theta_{beam} = \arcsin \left( \frac{\phi}{360^\circ} \frac{\lambda}{d} \right) \quad (5.1)$$

where  $\phi$  is the phase shift between adjacent elements in the array and in this case  $\lambda = 8.575 \times 10^{-3}$  m and  $d = 9.8 \times 10^{-3}$  m. As the test rig runs from  $0^\circ$  to  $180^\circ$ , the angle of the beam is centred around  $90^\circ$  and the above value of  $\theta_{beam}$  needs to be offset by  $90^\circ$ . This allows for the phase shift to be calculated to line up with the simulated results. The simulated results were then plotted against the theoretical beamshapes as well as a discretised version of the simulations in order to compare to the discrete data of the

## 5.2. EXPERIMENTAL RESULTS COMPARED TO SIMULATIONS

experiment results. These comparisons can be seen in Figure 4.1 and the individual plots can be found in the appendix. For comparison, the beam angle of each test can be found in Table 5.1.

Relative Phase $\phi$	Beam Angle $\theta$		
	Theoretical	Simulated	Discrete Simulated
0°	90°	90.1° ± 0.05°	90° ± 2.5°
45°	96.23°	95.4° ± 0.05°	95° ± 2.5°
-45°	83.72°	82.9° ± 0.05°	85° ± 2.5°
120°	106.96°	105.6° ± 0.05°	105° ± 2.5°

Table 5.1: Comparison of theoretical results to simulated results

It can be seen from this comparison that the simulated data does not agree with the theoretical results within experimental error. This is not unexpected as the theoretical shift assumes an omnidirectional transmitter with a uniformly emitted wave. As the transducers have a directional beam as seen in Figure 3.19, the expected constructive and destructive interference differs from what the theory expects. Despite this, the error between the theoretical and simulated data is less than 2° in the worst case, with a relative phase of 120°, and thus the simulated data can be shown to agree with the theoretical data despite the modifications to the transducers.

## 5.2 Experimental Results Compared to Simulations

In order to quantify the performance of the array, the measured beamshapes are compared to the simulations in two ways. Firstly, like in the comparison with the theoretical data, the angle of the main beam will be compared to assess the steering capabilities and accuracy of the array. Secondly, the shape of the main lobe will be compared as well as the magnitude and shape of any grating lobes.

### 5.2.1 Beam Angle

As the test rig only allowed 5° increments, the experimental results are only able to show the direction of the beam as pointing in a multiple of 5°. Figure 5.1 shows the average of the experimental results plotted against the simulations and the individual data can be found in Appendix C.

## CHAPTER 5. DISCUSSION

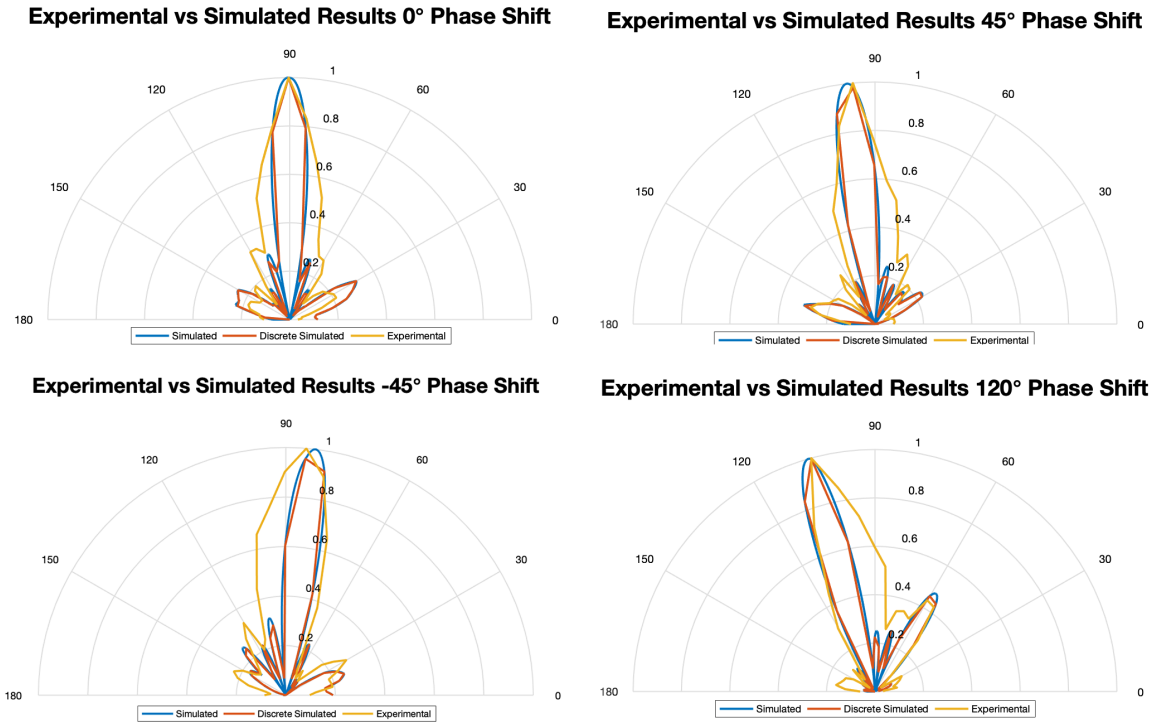


Figure 5.1: Simulated and experimental results of the array

For the sake of comparison, the resulting beam angle was tabulated with the simulated and theoretical values. This can be seen in Table 5.2 below.

Relative Phase $\phi$	Beam Angle $\theta$		
	Theoretical	Simulated	Experimental
0°	90°	90.1° ± 0.05°	90° ± 2.5°
45°	96.23°	95.4° ± 0.05°	95° ± 2.5°
-45°	83.72°	82.9° ± 0.05°	85° ± 2.5°
120°	106.96°	105.6° ± 0.05°	105° ± 2.5°

Table 5.2: Comparison of experimental results to simulated results

The results of the beam angle comparison show that the experimental angle is within agrees with the simulated data within experimental uncertainty. While these results are positive and show the array can be steered, the 5° increments of the test rig limit the precision of the results.

### 5.2.2 Beamshape

The main focus of the beamshape is the width of the main beam and the position and size of the grating lobes. As can be seen in Figure 5.1 in each case, the beamwidth of the experimental data is much wider than that of the simulated data. The causes of this discrepancies are not known, however, the increased amplitude must imply that the phase cancellation is not as destructive as the theory predicts. A possible cause of this is that the output amplitude of each modified transducer may not be consistent. The simulated results make use of the beamshape of the one measured modified transducer. Nevertheless, the widths of the simulated and experimental beams are tabulated in Table 5.3 below and the cross-correlation and mean squared error (MSE), of the normalised simulation and experimental data, of the beamshapes can be seen in Table 5.4. The normalisation allows for the MSE of each test to be easily compared to each other.

From Table 5.3 the measured beam width can be seen to be double that of the simulations. It is believed that this difference is due to the unknowns of the modified transducers, however, despite this discrepancy, the width of the steered beam is consistent throughout with a standard deviation of 15.0mm showing that this does not impact the performance of the beam steering but does impact the precision of the beam.

Table 5.4 attempts to show the similarity of the the simulated and experimental results. Both the cross-correlation and MSE results show that the signals are statistically similar. The MSE results show a very small error. This is due to the similarities of the majority of the grating lobes of the results. Due to the limited number of data points from the experimental results, the region of the beamshapes which most deviated from the simulated results only have a couple of data points which limits the MSE value. For similar reasons, the cross-correlation data is also unexpectedly high.

Relative Phase $\phi$	Beam Width (mm)	
	Simulated	Experimental
$0^\circ$	138	270
$45^\circ$	144	269
$-45^\circ$	138	285
$120^\circ$	135	260

Table 5.3: Comparison of experimental results to simulated results

Relative Phase $\phi$	Cross-Correlation	Mean Squared Error (V)
0°	0.908	0.0238
45°	0.907	0.0227
-45°	0.890	0.0326
120°	0.895	0.0273

Table 5.4: Cross-correlation between simulated and measured results

### 5.3 Performance of the Array

The results of the test show mixed success. The tests conclusively show that the beam is capable of being steered accurately. However, the expected beam is half the width of the experimental beam which means the scanned area is less precise. The impact of this depends on the application of the array.

Quantifying the performance of the array with the given data has proven to be difficult, however, by analysing all of the results together the performance can be addressed qualitatively. Firstly, the rough shape of the beam, the number of lobes and their relative amplitudes for the simulated data is similar to the experimental data. A more analytical comparison is the direction of the main and grating lobes agree with the simulations within experimental uncertainty. The width of the beamshape shows that the data is not the same as the simulations, however, as the beam width was consistent, the predicted output is still clearly determinable.

The results tend to show that the error is most significant in the case of the -45° or 315° shift. This is likely as a result of the phase shifters causing distortion towards the end of their range.

Despite all of this, the array is able to output a beam with constant beamwidth which can be steered reliably by the control voltages. This is considered to be a good performance of the array despite the differences from the simulations.

# Chapter 6

## Conclusions

This report began by outlining the task which needed to be solved. The report researched existing projects in order to gain insight into a solution. This lead to the design being split into three subsections. The subsections consisted of phase shifting at 40kHz, powering the beam from the output of the phase-shifter and the beamforming of the four-element array.

The phase shifting units were designed to be controlled by a DC control voltage allowing the array to be steered using a microcontroller. The phase shifting units made use of concepts from audio signal processing applications in order to achieve a full  $0^\circ$  to  $360^\circ$  phase shift. The experimental testing of the phase-shifters shows that, despite some attenuation, they are able to create the desired shift. The phase-shifters did however suffer from controllability issues as the tested units did not have a linear response to the control voltage. This did not hinder the testing of the system, however this design is not recommended without modifications. Possible solutions to this are discussed below.

The phase-shifting units were then fed into the transducer driver circuitry which was constructed using a comparator in order to convert the sinusoid which was required for the phase-shifting units into a square wave of identical phase required for to power the transducers. The beamforming began by modifying the available transducers in order to fit them close enough together to avoid large grating lobes from forming. This allowed an array of four elements to be constructed.

The results of the experimental studies show that the project was successfully able to design and construct an AESA-style phased array transmitter using ultrasonic transponders. The experimental tests show that the angle to which the beam is steered is within

## CHAPTER 6. CONCLUSIONS

experimental error of the expected values while the beam width is wider than expected. Despite this, the array was determined to have performed well as a proof of concept.

This study acts as a proof-of-concept for an ultrasonic phased array being used for ranging and detection. The methods described in this report enable the array to be expanded in size, dimension and frequency in order to provide more useful applications. This report also shows the feasibility for a low-cost, low-power array which can be almost infinitely scaled without significant resources.

# Chapter 7

## Recommendations

The obvious recommendation which can be made is that, since this report forms the first part of a two-part investigation, the second part of the investigation can be studied based on the results of this report. Part two of this acoustic AESA project involves the receiver side of the phased array making use of digital beamforming to determine the angle of a received wave.

As the phase-shifting units caused distortion towards the extremes of their phase sweeps, each phase shifter could be constructed with an addition  $0^\circ$  -  $90^\circ$  all-pass filter to increase the range of the sweeps and reducing the need to sweep to the extremes.

Further study can also be conducted into different ways to control the phase shift. The attenuation of the phase shift circuitry was caused by the JFETs used. As the JFETs simply provide a variable resistance, they could be replaced with other components such as varistors and LDRs which may provide a more linear control with no attenuation.

This project constructed a 1-Dimensional array with four elements. The modular nature of the construction of the circuitry allows the project to be expanded to attempt to build a 2-Dimensional array capable of steering the beam in two directions. The addition of transducers to increase the number of elements can also be investigated.

The theory applied to the frequency of the ultrasound should scale upwards. This can allow ultrasound to be used over an increased range making the system better suited to be used as a ranging and detection device. Similarly, the array could be tailored to be used as a low-cost non-intrusive medical imaging tool.

# References

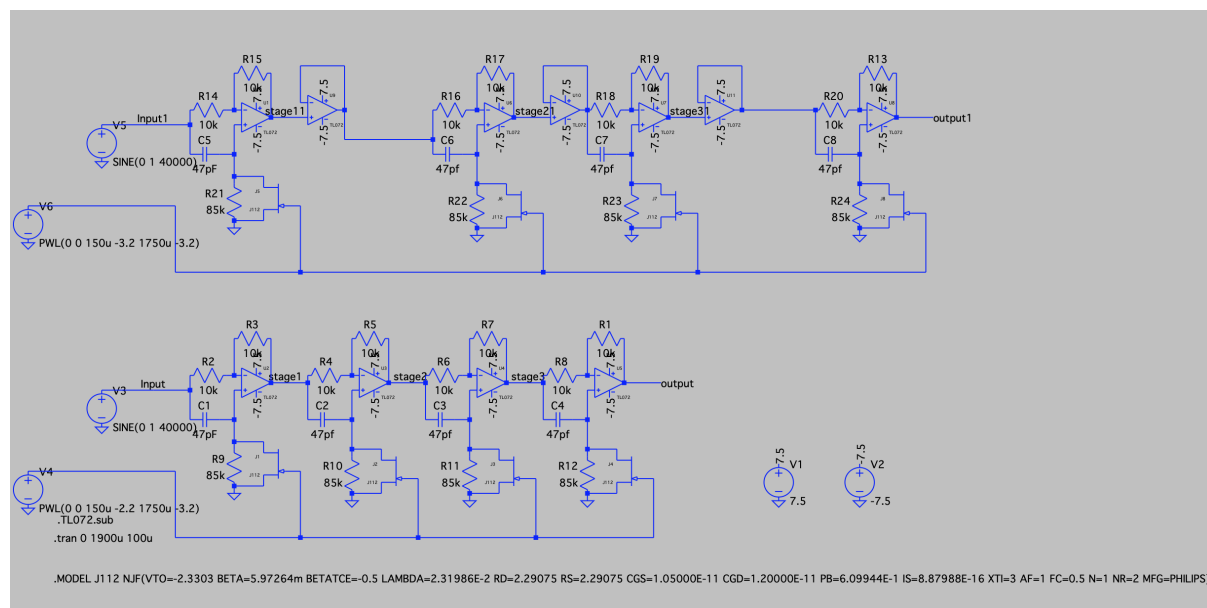
- [1] W. L. Stutzman and G. A. Thiele, *Antenna Theory and Design*. John Wiley Sons, 1998.
- [2] A. J. Fenn, D. H. Temme, W. P. Delaney, and W. E. Courtney, “The development of phased-array radar technology,” *Lincoln Laboratory Journal*, vol. 12, no. 2, pp. 321–340, 2000.
- [3] Panasonic, “BBD Bucket Brigade Devices.”
- [4] Texas Instruments Inc, “LM311 Differential Comparator,” September 1973, revised March 2017.
- [5] C. for Devices and R. Health, “Ultrasound imaging.” [Online]. Available: <https://www.fda.gov/radiation-emitting-products/medical-imaging/ultrasound-imaging>
- [6] D. Keepots, “Phase shifting and the beating of complex waves,” *Physics Education*, vol. 46, no. 2, pp. 187–190, 2011.
- [7] R. Keen, “The technology of phase shifters and flangers,” 1999. [Online]. Available: [http://www.geofex.com/article\\_folders/phasers/phase.html](http://www.geofex.com/article_folders/phasers/phase.html)
- [8] Mobicon Electrical Components, “UT1612MPR Ultrasonic Sensor,” prepared By: Leo Wong.
- [9] D. Han, J. Huang, J. Zhou, M. Wang, S. Xu, H. Li, and S. Li, “Multi-field-coupled model and solution of active electronically scanned array antenna based on model reconstruction,” *International Journal of Antennas and Propagation*, vol. 2018, 2018.
- [10] A. Macovski, “Ultrasonic imaging using arrays,” *Proceedings of the IEEE*, vol. 67, no. 4, pp. 484–495, 1979.
- [11] N. Wagner, Y. C. Eldar, and Z. Friedman, “Compressed beamforming in ultrasound imaging,” *IEEE Transactions on Signal Processing*, vol. 60, no. 9, pp. 4643–4657, 2012.

- [12] D. R. D. Hynynen and Kullervo, “A 256-element ultrasonic phased array system for the treatment of large volumes of deep seated tissue,” *ieee transactions on ultrasonics, ferroelectrics, and frequency control*, vol. 46, no. 5, pp. 1254–1265, 1999.
- [13] I. K. Holfort, F. Gran, and J. A. Jensen, “Broadband minimum variance beamforming for ultrasound imaging,” *IEEE Trans Ultrason Ferroelectr Freq Control*, vol. 56, no. 2, pp. 314–25, 2009. [Online]. Available: <https://www.ncbi.nlm.nih.gov/pubmed/19251518>
- [14] A. P. Malvino and D. J. Bates, *Electronic Principles*. McGraw-Hill Education, 2016.
- [15] Electrosmash, “Mxr phase 90 analysis,” 2013. [Online]. Available: <https://www.electrosmash.com/mxr-phase90>
- [16] ——, “Bucket brigade devices: Mn3007,” 2017. [Online]. Available: <https://www.electrosmash.com/mn3007-bucket-brigade-devices>
- [17] Princeton Technology, “PT2399 Echo Processor IC,” February 2010, v1.6.
- [18] D. Wolfe, “The global shortage of capacitors impacts all consumer electronics,” 2019. [Online]. Available: <https://qz.com/1575735/a-mlcc-shortage-is-stifling-electronics-hardware-auto-makers/>
- [19] Siliconix, “FETs as voltage-controlled resistors an105,” pp. 1–6, March 1997.
- [20] R. Keen, “JFET matching for effects,” 2002. [Online]. Available: [http://www.geofex.com/article\\_folders/fetmatch/fetmatch.htm](http://www.geofex.com/article_folders/fetmatch/fetmatch.htm)
- [21] runoffgroove.com, “JFET tester v2.0,” 2008. [Online]. Available: <http://www.runoffgroove.com/fetzertech10.png>
- [22] “Ultrasonic proximity detector.” [Online]. Available: <https://www.jameco.com/Jameco/workshop/JamecoFavorites/proximity.html>

# Appendix A

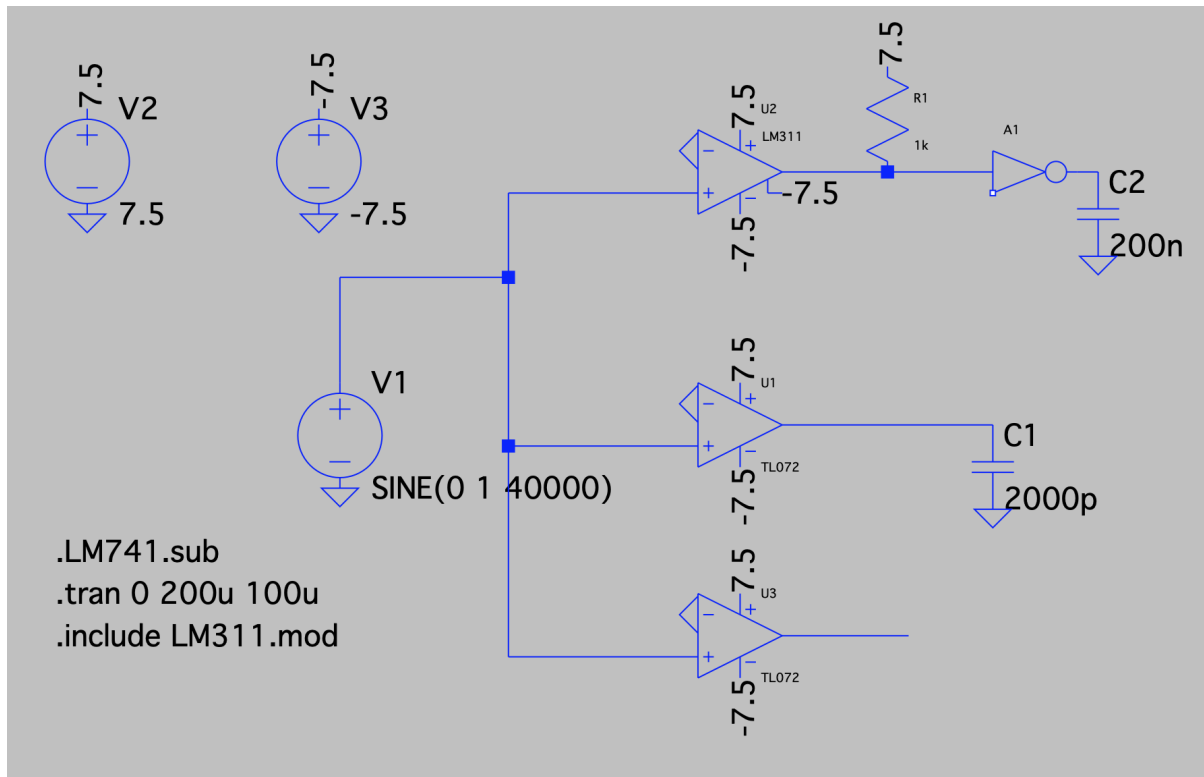
## SPICE Models

### A.1 Phase Shifting Units



SPICE simulation in LTSpice of the phase shifters

## A.2 Driver Circuitry

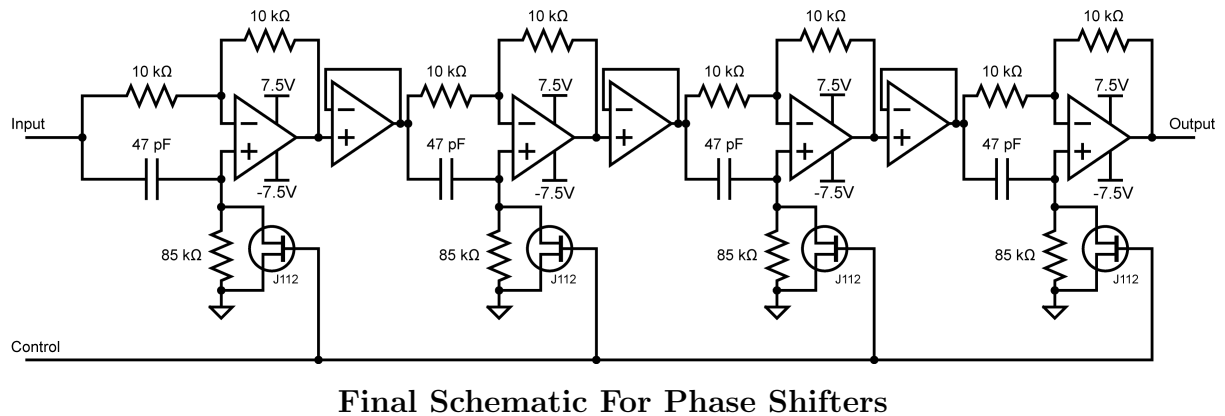


SPICE simulation in LTSpice of the driver ciruity

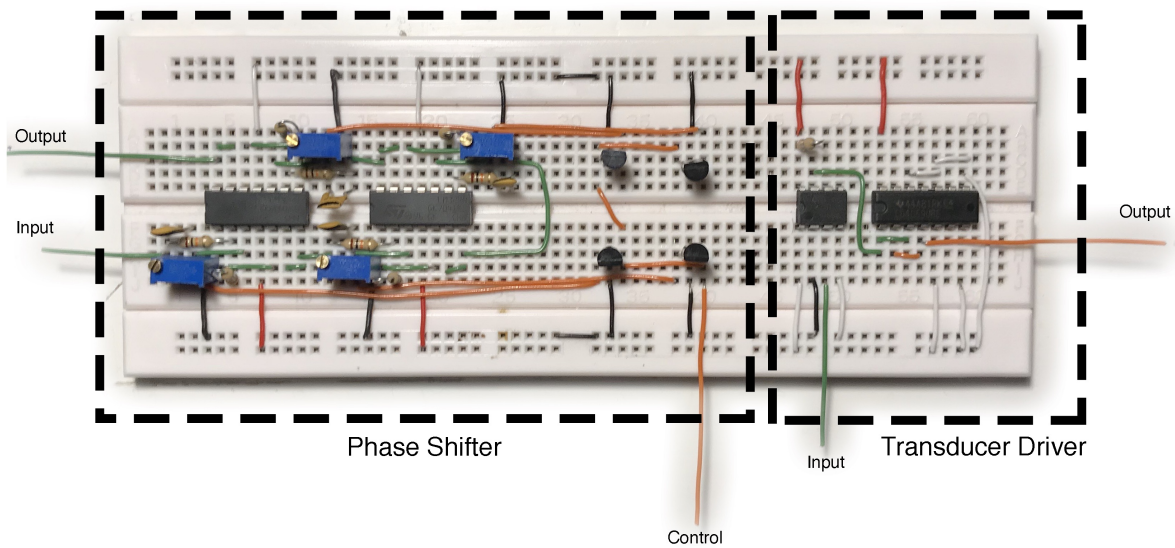
# Appendix B

## Schematics and Layouts

### B.1 Schematics

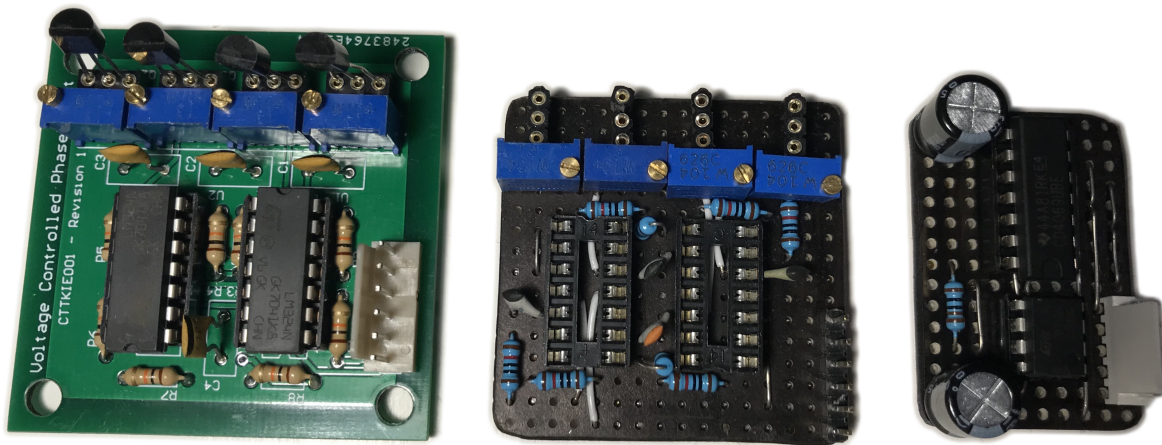


## B.2 Breadboard Layouts



Breadboard layout of phase shifter and transmitter driver

## B.3 PCB and Veroboard Layouts



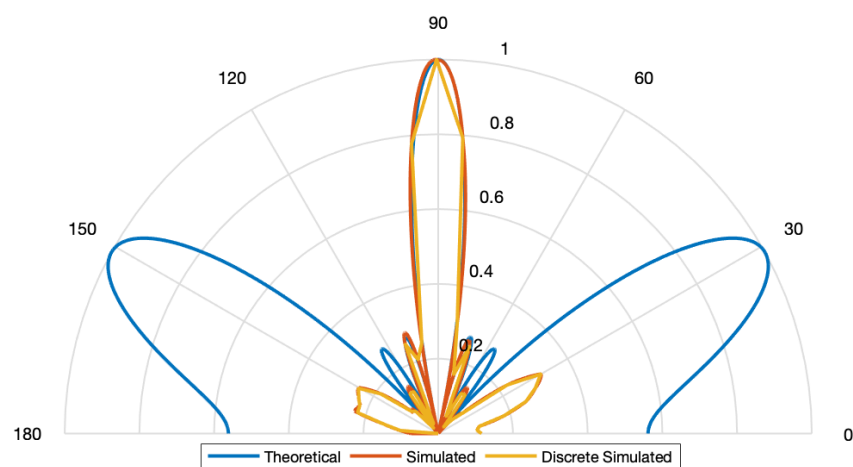
PCB layout of phase shifter, Veroboard layout of phase shifter, Veroboard layout of transmitter driver

# Appendix C

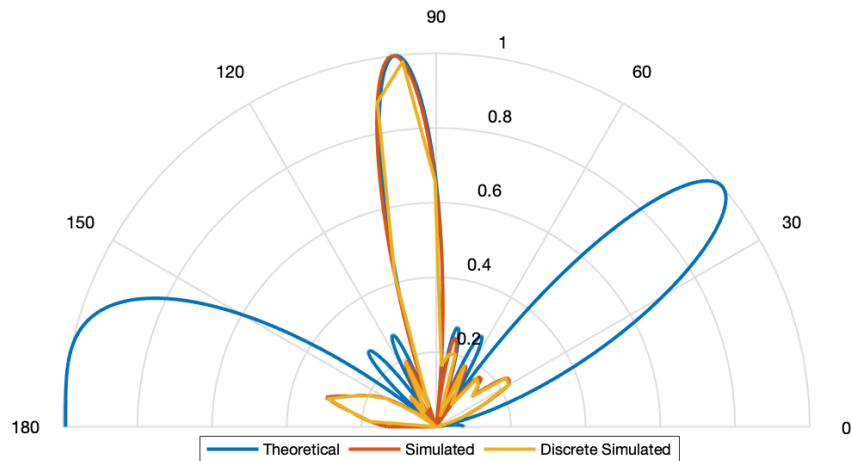
## Additional Results & Resources

### C.1 Simulation Results

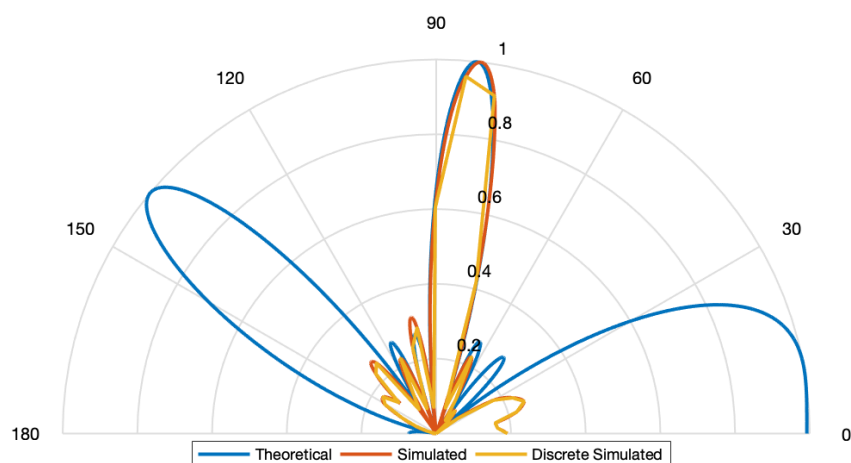
**Theoretical vs Simulated Results 0° Phase Shift**



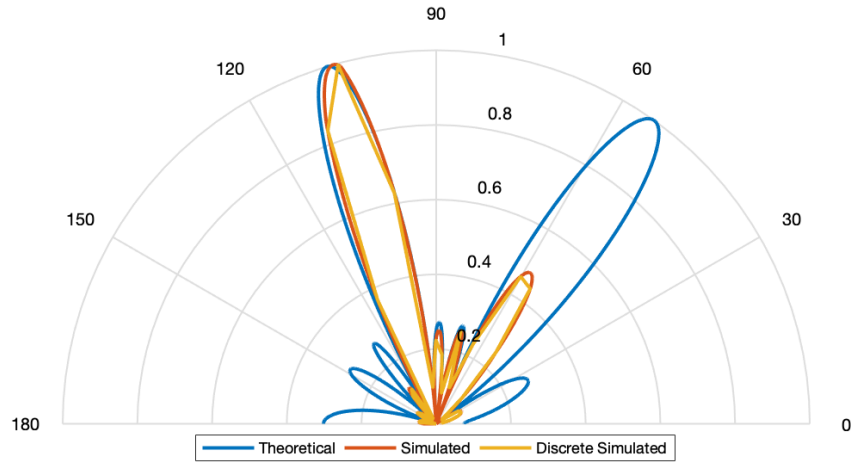
**Theoretical vs Simulated Results 45° Phase Shift**



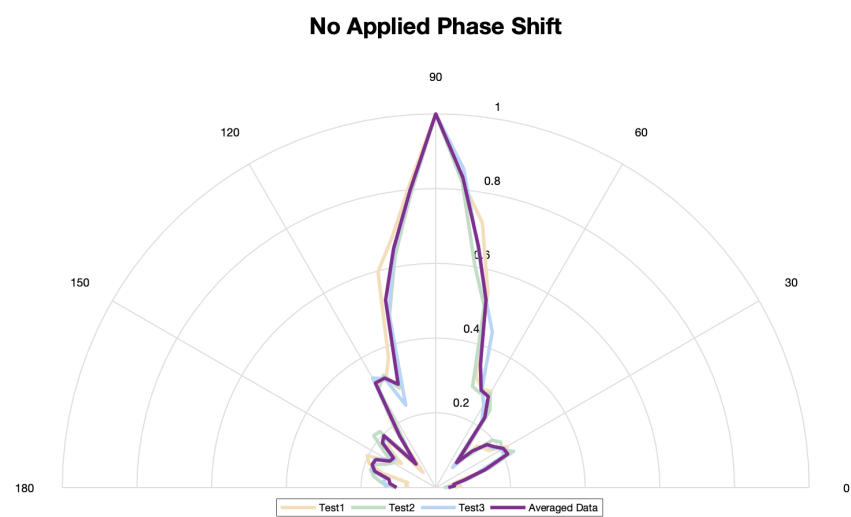
**Theoretical vs Simulated Results -45° Phase Shift**



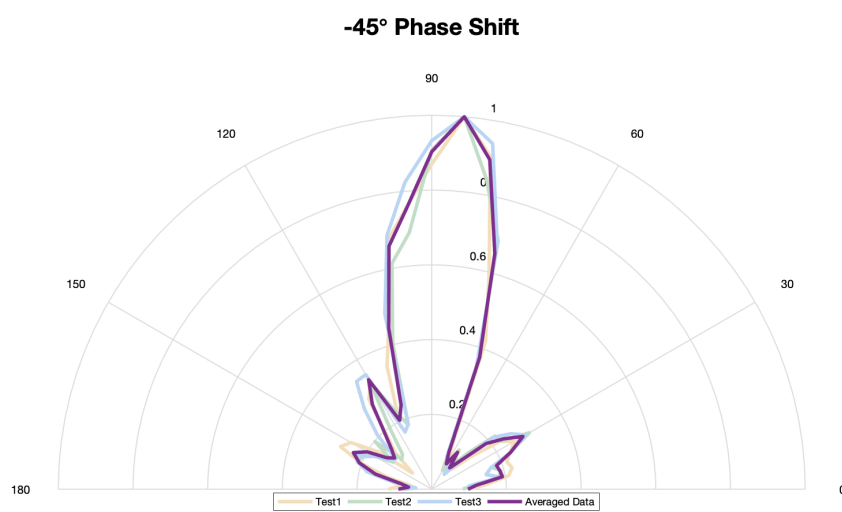
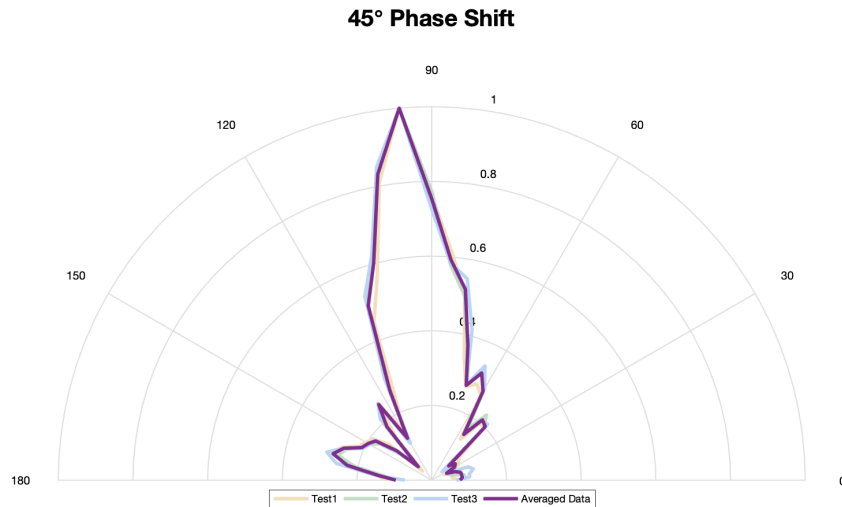
### Theoretical vs Simulated Results 120° Phase Shift

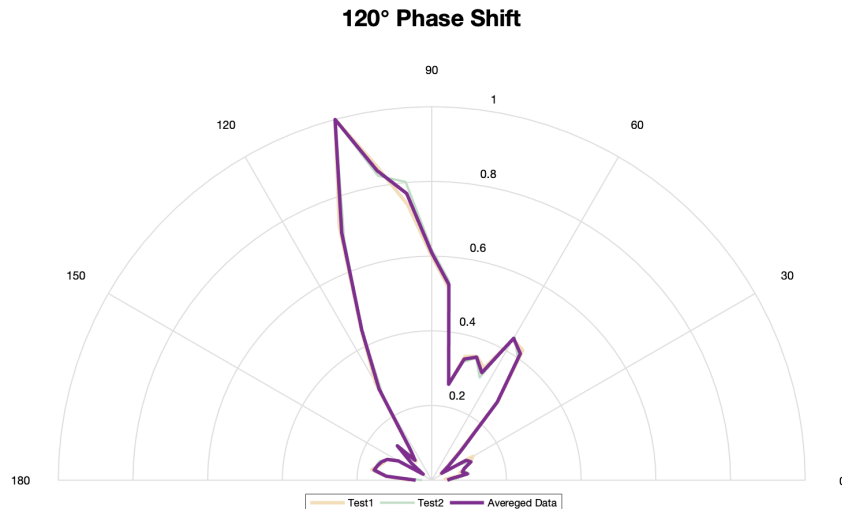


### C.2 Experimental Results



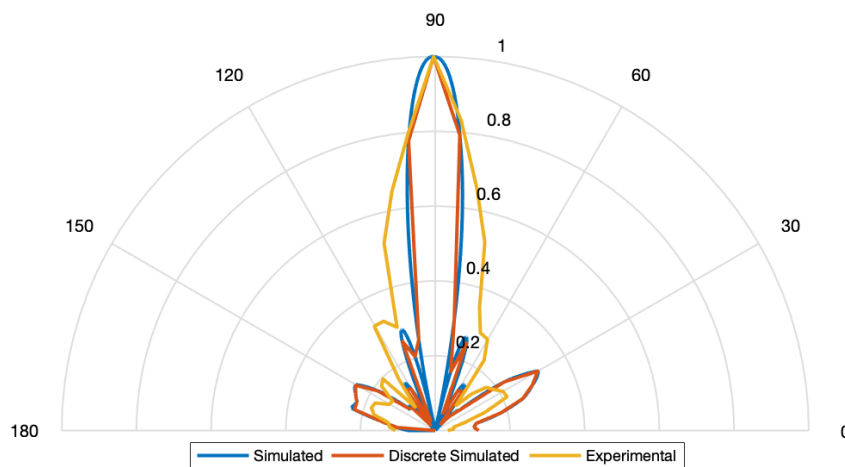
## C.2. EXPERIMENTAL RESULTS

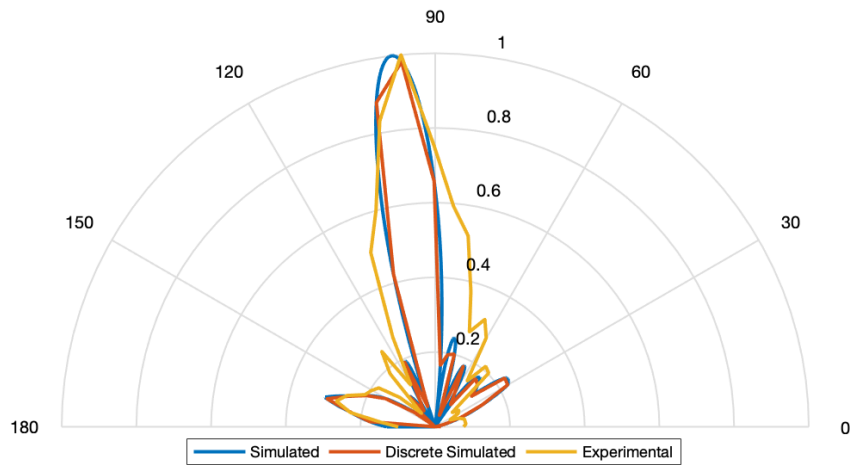
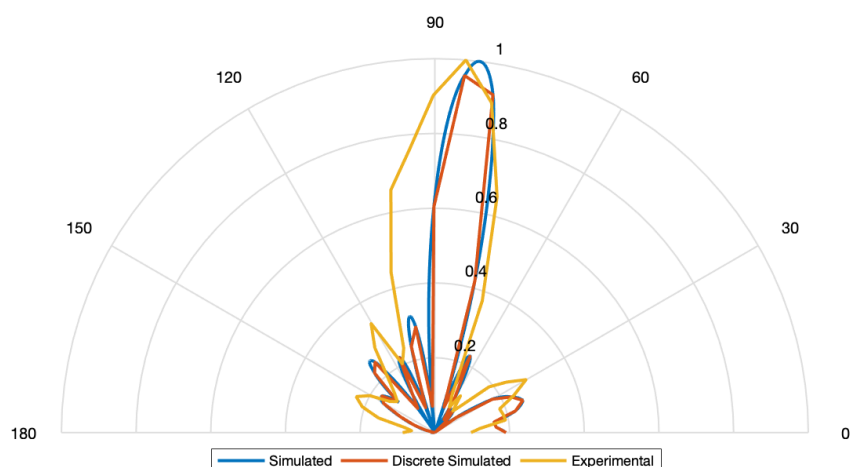




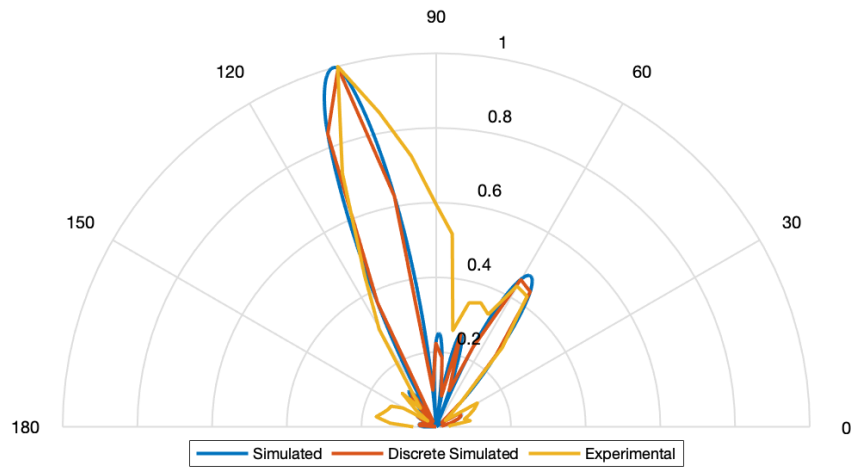
### C.3 Comparisons

**Experimental vs Simulated Results 0° Phase Shift**

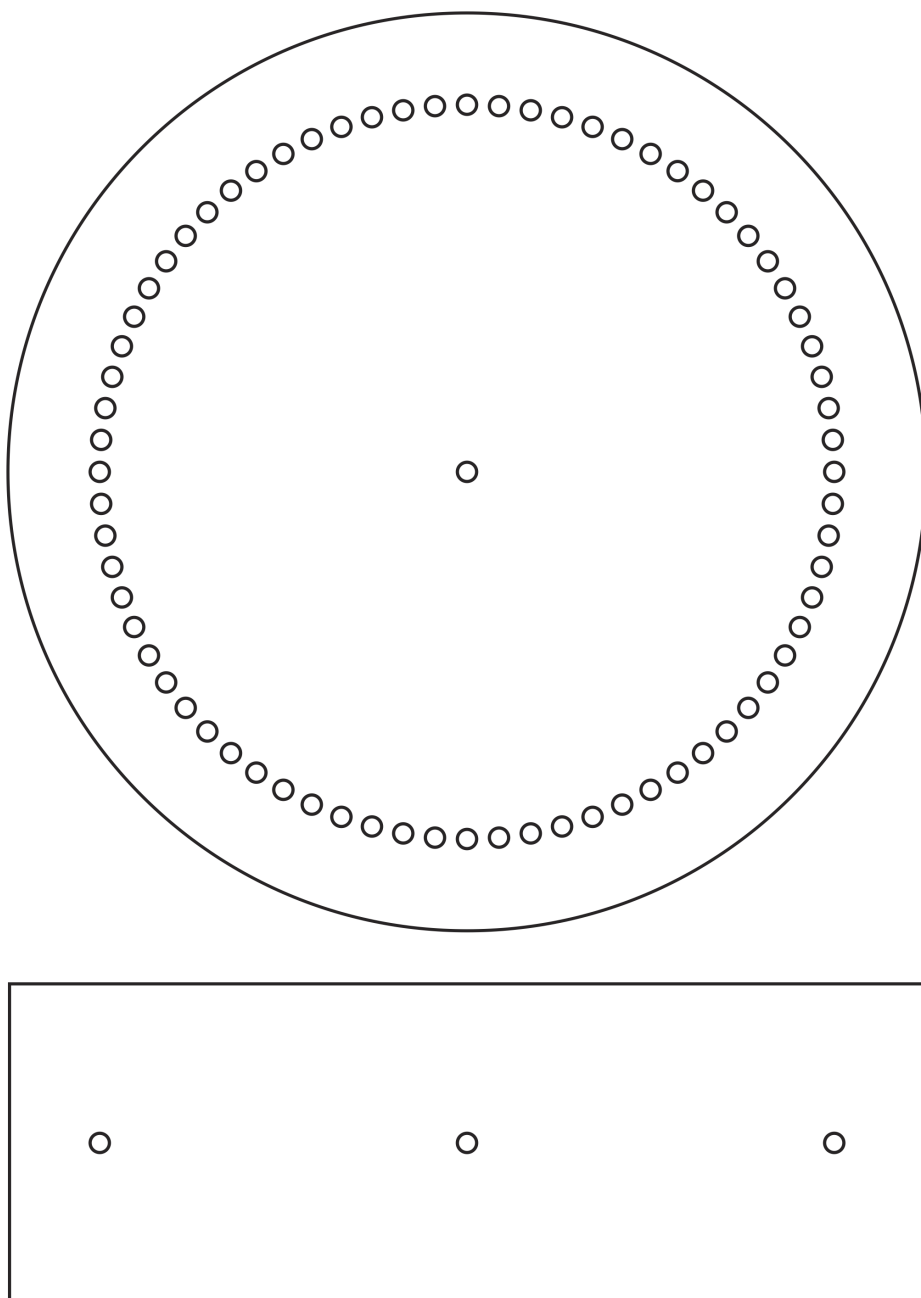


**Experimental vs Simulated Results 45° Phase Shift****Experimental vs Simulated Results -45° Phase Shift**

### Experimental vs Simulated Results 120° Phase Shift



## C.4 Test Rig Laser Cutting Template

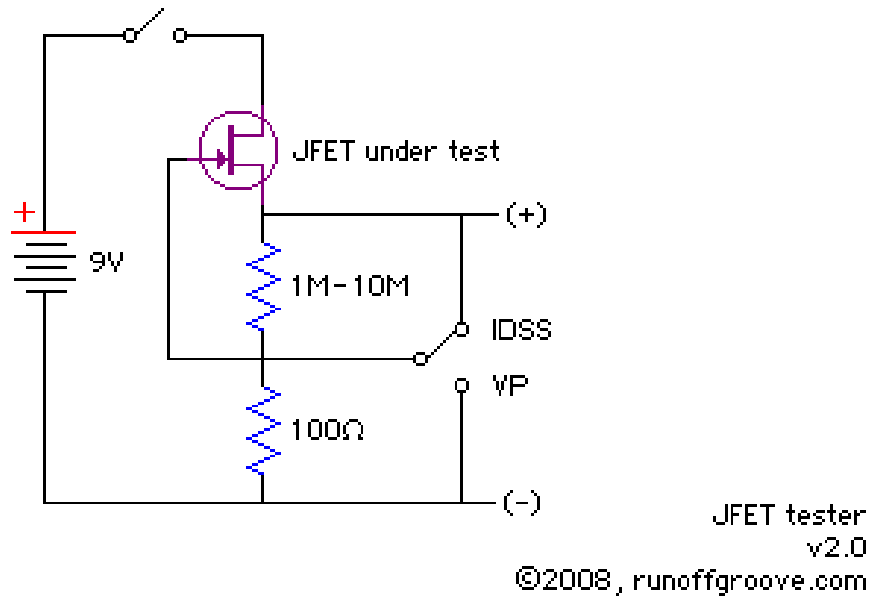


Laser Cutting template of the test rig

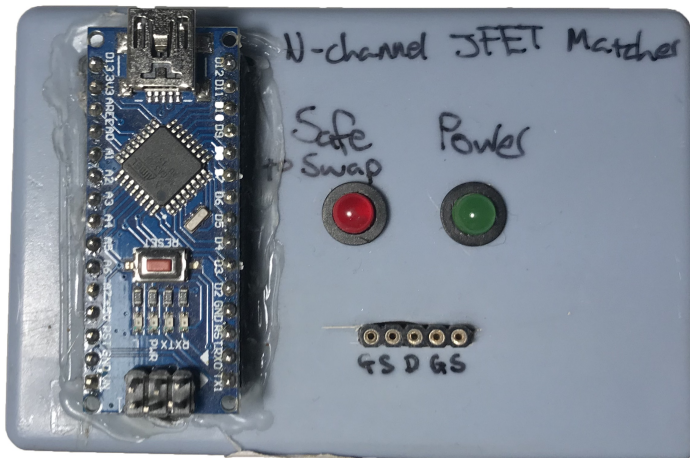
## C.5 JFET Matching Circuit

### OPERATING INSTRUCTIONS:

1. Connect digital multimeter set for DC voltage to test points (+) and (-)
2.  $Id_{SS}$  reading: switch to  $Id_{SS}$  mode and multiply measured voltage by 10 for  $Id_{SS}$  in mA
3.  $V_p$  reading: switch to  $V_p$  mode and measured voltage directly corresponds to  $V_p$



Schematic used to check JFET characteristics. Image taken from [21]



Arduino implementation of above schematic. The Arduino simply reads the analogue voltage

# **Appendix D**

## **MATLAB Code**

All of the relevant calculations and functions can be found at the link below

<https://github.com/KieranCattellUCT/FinalYearProject>



# Appendix E

## Ethics Form

### EBE Faculty: Assessment of Ethics in Research Projects

Any person planning to undertake research in the Faculty of Engineering and the Built Environment at the University of Cape Town is required to complete this form before collecting or analysing data. When completed it should be submitted to the supervisor (where applicable) and from thence to the Head of Department. If any of the questions below have been answered YES, and the applicant is NOT a fourth year student, the Head should forward this form for approval by the Faculty EIR committee: submit to Ms Zulpha Geyer ([Zulpha.Geyer@uct.ac.za](mailto:Zulpha.Geyer@uct.ac.za); Chem Eng Building, Ph 021 650 4791). Students must include a copy of the completed form with the final year project when it is submitted for examination.

Name of Principal Researcher/Student:	KIERAN CATTELL	Department:	ELECTRICAL ENGINEERING		
If a Student:	YES	Degree:	BSc Eng MECHATRONICS	Supervisor:	WPF SCHONKEN
If a Research Contract indicate source of funding/sponsorship:	NO				
Research Project Title:	Acoustic AESA Project 1: Transmitter Design & Anagloue Beamforming				

Overview of ethics issues in your research project:

Question 1: Is there a possibility that your research could cause harm to a third party (i.e. a person not involved in your project)?	YES	<input checked="" type="radio"/> NO
Question 2: Is your research making use of human subjects as sources of data? If your answer is YES, please complete Addendum 2.	YES	<input checked="" type="radio"/> NO
Question 3: Does your research involve the participation of or provision of services to communities? If your answer is YES, please complete Addendum 3.	YES	<input checked="" type="radio"/> NO
Question 4: If your research is sponsored, is there any potential for conflicts of interest? If your answer is YES, please complete Addendum 4.	YES	<input checked="" type="radio"/> NO

If you have answered YES to any of the above questions, please append a copy of your research proposal, as well as any interview schedules or questionnaires (Addendum 1) and please complete further addenda as appropriate.

I hereby undertake to carry out my research in such a way that

- there is no apparent legal objection to the nature or the method of research; and
- the research will not compromise staff or students or the other responsibilities of the University;
- the stated objective will be achieved, and the findings will have a high degree of validity;
- limitations and alternative interpretations will be considered;
- the findings could be subject to peer review and publicly available; and
- I will comply with the conventions of copyright and avoid any practice that would constitute plagiarism.

Signed by:

	Full name and signature	Date
Principal Researcher/Student:	Kieran Cattell	13 October 2019

This application is approved by:

Supervisor (if applicable):	WPF Schonken	13 October 2019
HOD (or delegated nominee): Final authority for all assessments with NO to all questions and for all undergraduate research.	Janine Buxey	13 October 2019
Chair : Faculty EIR Committee For applicants other than undergraduate students who have answered YES to any of the above		